Blue BX Galaxies Breaking Bad:

Allegations of a 2175Å feature at $z \sim 2.2$ in violation of the Calzetti dust law

by

Anneya Golob

A Thesis Submitted to

Saint Mary's University, Halifax, Nova Scotia

in Partial Fulfillment of the Requirements for

the Degree of Master of Science in Astronomy

(Department of Astronomy and Physics)

January 14, 2013, Halifax, Nova Scotia

© Anneya Golob, 2013

Approved: Dr. Marcin Sawicki
Supervisor

Approved: Dr. Luigi Gallo
Examiner

Approved: Dr. Robert Thacker
Examiner

Date: January 14, 2013

Acknowledgements

I offer my most sincere thanks to my supervisor, Dr. Marcin Sawicki. Your guidance in this endeavour has been invaluable. I have learned much more about data reduction, analysis, statistics, and research in general than I could have hoped. I look forward to working with you in the future.

Many thanks to the distinguished members of my committee Dr. Luigi Gallo and Dr. Rob Thacker for their patience in the completion of this work and for their insighful suggestions on ways to improve and further it.

Thanks to my parents for unconditional love and support through thick and thin, well-timed care packages with all the right candy, and excellent medical insurance.

I must express infinite appreciation for my fellow inhabitants of the grad-student zoological exhibit: to Liz, Bobby, Michael, Dave, James, Larkin, John, T.P.T., Chris, Kirsten, Chris, Sherry, Mitch and Lambert, without the academic collusion and commiseration we've shared, we'd all be lost.

Special thanks to Jay for many living room dance parties and conversations in reciprocally broken spanish, to Patrick/Ryan Fortier for titillating lexiphanic and philosophical rhetoric, and to Diego for endless emotional support, collaborative soups, funny voices, and so many other things, ineffable in any language.

Contents

List of Figures

List of Tables

Abstract

Blue BX Galaxies Breaking Bad

by Anneya Golob

The dust properties of star forming galaxies at $z \sim 2$ are examined using a sample of BX objects selected from the Keck Deep Fields (KDF) using colour-colour selection criteria. Spectral energy distribution (SED) fitting is used to infer physical properties of these galaxies from $U_nG\mathcal{R}IHK_s$ photometric data. Results suggest that the spectra of many of the BX objects with blue rest-frame UV colours include a 2175Å absorption feature not conventionally considered in high redshift analyses. The redshift ranges over which SEDs exhibiting the feature satisfy the BX selection criteria are computed and found to vary significantly between models including different dust laws. Clustering analyses are shown to be sensitive to the assumed dust attenuation law. Inappropriate dust model choices may lead to factor-of-two overestimates of spatial correlation lengths. The possibility of using the 2175Å feature as a redshift indicator is investigated through tests on synthetic galaxy photometry with promising results.

January 14, 2013

Chapter 1

Introduction

The faint light of distant populations of galaxies among the first to form in the universe is only now arriving at our telescopes. By peering back in time at these early settlers, we stand to learn much about cosmology, large-scale structure and the formation and evolution of galaxies that produced the conditions we observe locally. We also find invaluable evidence that is useful in refining and constraining the theoretical models we use to further our knowledge of the processes occurring on scales too small or large to observe with ease. Observational technology is constantly improving, allowing us to probe further into the history of the universe. However, the complexity of the task means that the technological challenges of observing the high-redshift universe are far from surmounted.

1.1 Photometric Selection of High Redshift Galaxies

The principal challenge in collecting data from high redshift galaxies is how faint they appear from our vantage point. It is certainly possible to point a telescope at a single object for days (or perhaps years, depending on the wavelength of observation) on end to collect enough light to spectroscopically measure its redshift and resolve it to determine its morphology. However, this is generally impractically expensive and data from a single object are insufficient to infer anything

about the ancient universe in general. Large samples of galaxies are required to observe trends in populations of high redshift objects.

The need for such samples prompted the development of photometric selection methods which identify objects likely to fall in a redshift range from observations in only a few filters. These techniques exploit prominent features in galaxy spectra. Figure 1.1 shows the typical spectrum of a star-forming galaxy at redshift 2.2 with the transmission functions of filters used in the Keck Deep Fields (hereafter KDF) observations described in Section 2. The two most notable features in the spectrum are the Lyman limit at (rest frame) 912Å and the Balmer/4000Å break. Photons with energies higher than the Lyman limit are almost completely absorbed by the abundant neutral gas in star forming regions. The few photons that do escape are subject to absorption by intergalactic hydrogen along the line of sight which create the Lyα forest. The first highly successful photometric selection method relied on filters straddling the position of the Lyman break (Guhathakurta et al. 1990; Steidel et al. 1995, 1996). If a galaxy has an extreme red colour between the two filters, the Lyman limit at the galaxy's redshift is likely to fall between the central wavelengths of the filters. This technique for selecting Lyman break galaxies (LBGs) has been confirmed spectroscopically and extended to higher redshifts by using different filter combinations (Iwata et al. 2007; Lee et al. 2006; Ouchi et al. 2004). The Balmer/4000Å break can be used in the same way, however it is not present in young, actively star forming galaxies (Calzetti et al. 2000).

The Lyman break selection criteria rely on data from just three filters and have proven their worth in selecting large samples of galaxies in a given redshift range. They cannot, however, be relied upon to accurately determine the redshift of an individual object. Considering data at more than three wavelengths allows better sampling of a galaxy's spectrum and can thus be used to better estimate its redshift. This technique of interpolating the shape of an object's spectral energy distribution (SED) from a set of broadband observations is known as photometric redshift determination and amounts to very low-resolution spectroscopy. In this method, observations of the flux from an object at any number of wavelengths are compared to a grid of model galaxy spectra with known parameters. SED fitting of this type can be used to determine not only the redshift of an object, but,

Figure 1.1: Typical spectrum of a star forming galaxy at redshift 2.2 and the transmission functions of the filters used in the KDF observations. Filter transmission curves were obtained from the Keck LRIS and Gemini NIRI instrument websites. The locations of the Lyman break (at rest-frame 912Å) and the Balmer/4000Å break are noted.
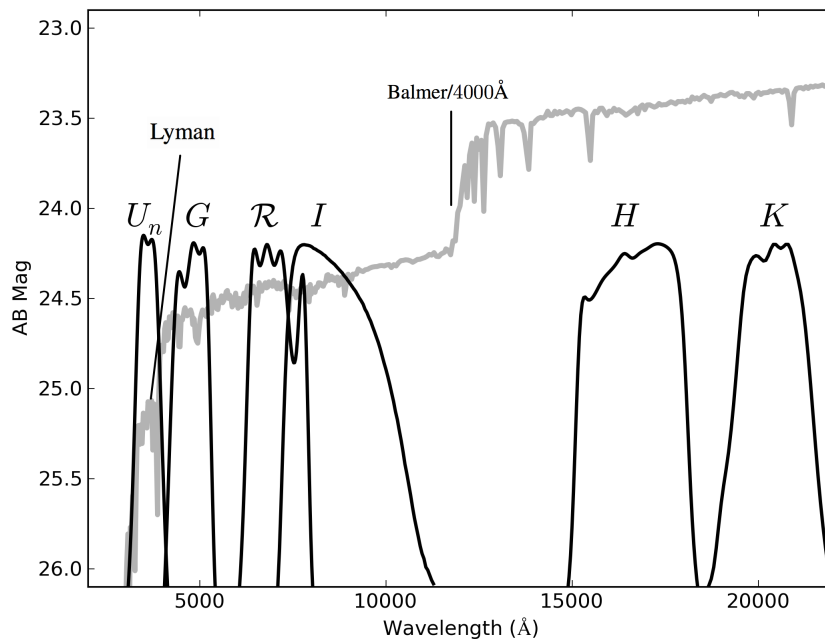
with sufficient sampling of its SED, other properties such as its mass, age, and rate of star formation (e.g. Walcher et al. 2006; Salim et al. 2009).

Relatively few galaxies have been identified in the redshift range $1 < z < 3$. Below $z \sim 1$ magnitude-limited surveys can be used and at $z > 3$, the Lyman break technique becomes effective. The spectra of galaxies between these redshifts have no visible spectral breaks at optical wavelengths and are thus very difficult to identify from ground-based observatories. The lack of breaks in these spectra can itself serve as a useful diagnostic, but to conclusively rule out the presence of breaks, observations at a minimum of five wavelengths are necessary.

Photometric redshift techniques are computationally intensive so it is useful to have a rough idea of the redshift of an object from simple selection criteria before investing in subsequent observations and SED fitting. Adelberger et al. (2004) found that it is possible to identify star-forming galaxies at $z \sim 2.2$ using $UG\mathcal{R}$ observations with minimal contamination from foreground interlopers. This population of galaxies, known as BX objects, is scrutinized in this work. They are defined by their location in the trapezoidal region in the *(U-G)* *(G-$\mathcal{R}$)* plane defined by

$$G - R \geq -0.2$$
$$U_n - G \geq G - R + 0.2$$
$$G - R \leq 0.2(U_n - G) + 0.4$$
$$U_n - G \leq G - R + 1.0 \tag{1.1}$$

and shown by the shaded regions in Figure 1.2. In this work, the class of BX objects is separated into regular and blue BX (bBX) galaxies where the bBX population satisfies U-$G \leq 0.0$.

Figure 1.2: The grey shaded region of the *(U-G)* *(G-R)* corresponding to the BX selection criteria for $z \sim 2.2$ galaxies as defined by Equation 1.1. The darker region represents the region which defines the blue BX (bBX) galaxies considered in this work with *U-G* ≤ 0.0.
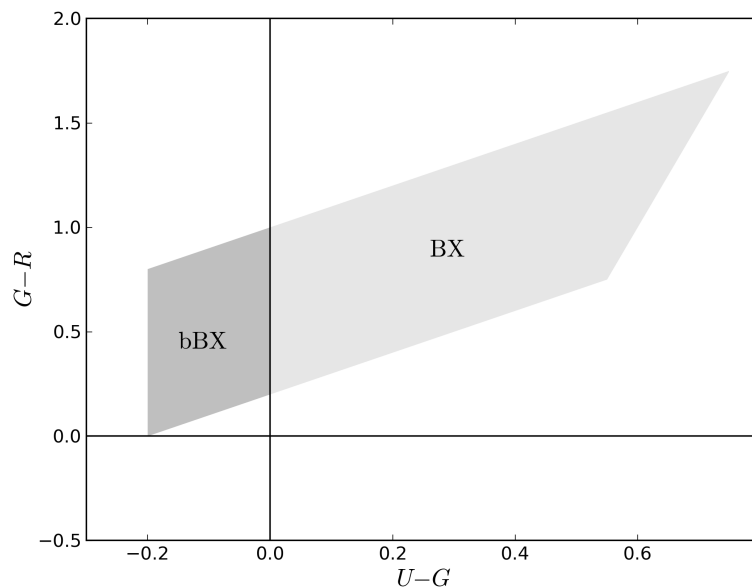
1.2   The Keck Deep Field

The BX selection criteria have been extensively tested with spectroscopic observations of objects which provide an independent measurement of their redshifts. Steidel et al. (2004) conducted a robust test of the method by examining the spectroscopic redshifts of 749 BX galaxies culled from seven multiwavelength surveys. In the group of the brightest objects in the sample, with $19.0 < \mathcal{R} < 22.0$, 84.6% of BX-selected objects were actually located at $z < 1$. The fraction of foreground interlopers decreases for fainter subsamples so that in the faintest bin, with $25.0 < \mathcal{R} < 25.5$, it was just 1.9%. The work of the Steidel team has shown the effectiveness of the BX-selection criteria for bright objects but their data were not deep enough to measure the faint end of the luminosity function at the high redshifts under consideration. The need for more faint objects was the motivation for the Keck Deep Fields (hereafter KDF) described by Sawicki & Thompson (2005). The survey used the same filters as the Steidel collaboration to obtain deep $UG\mathcal{R}I$ observations with a completeness limit of $\mathcal{R}_{lim} \sim 27$. Colour-colour selection techniques

were applied to objects identified in the field to construct samples of very faint star forming galaxies at $z \sim 4$, 3, 2.2, and 1.7. The data from the survey were used to study the redshift evolution of the following properties of galaxy populations: the rest-frame 1700Å luminosity function (Sawicki & Thompson 2006a), star formation and luminosity densities (Sawicki & Thompson 2006b), and clustering strength (Savoy et al. 2011). Possible properties of blue BX galaxies inferred from the clustering analysis prompted the IR observations and analysis described in this work.

1.3 Statistical Clustering

The distribution of galaxies in the universe traces the underlying distribution of dark matter (DM). The most massive DM halos exert the greatest gravitational force on baryonic matter and are thus home to more massive galaxies. The clustering strength (a measure of the overdensity in the spatial distribution of members of a population compared to a random distribution) of dark matter haloes is known to correlate with mass, thus both the most massive galaxies and dark haloes are the most strongly clustered. (Mo et al. 1996)

By identifying overdensities in the distribution of galaxies at increasing distances and examining their properties, it is possible to follow the evolution of structure in the universe and to gain insight into the interplay between the formation of galaxies from baryonic matter and the dark matter that supports them. Savoy et al. (2011) use the KDF data to do just this. After the objects identified in the KDF survey were divided by probable redshift using colour-colour selection methods, the distribution of each population on the sky was examined to measure its spatial clustering strength.

Savoy et al. (2011) found that at $z \sim 4$ and 3, UV bright galaxies were more strongly clustered than UV faint ones, consistent with previous studies, but that the reverse may be true by $z \sim 1.7$. This would imply some transitional effect in the $z \sim 2.2$ population. They interpret this as evidence in favour of galaxy downsizing: between $z \sim 3$ and $z \sim 1.7$ the sites with the greatest star formation activity migrate from high-mass DM haloes to those with lower mass. The KDF redshift samples were further divided by rest frame UV colours. In these samples, clustering was found to be strongest

in the galaxies with blue UV colours at $z \sim 4$, 3, and 2.2, but the trend was not observed at $z \sim 1.7$. In fact, the data were consistent with its reversal. The strongest dependence of clustering on colour was observed at $z \sim 2.2$. If the trend does indeed reverse and the galaxy downsizing hypothesis is correct, it is possible that the galaxies observed at $z \sim 2.2$ are in the process of shutting down star formation. It is well known that the star formation rate in the universe at large peaked around $z = 2$ and has since been declining (Madau & Pozzetti 1998; Hopkins & Beacom 2006). The conditions that caused this change are not well understood so insight into this critical period in the history of the universe is tantalizing.

Savoy et al. (2011) suggested the possibility that the strong colour dependence of clustering is the result of the 2175Å absorption bump observed along most sight lines in the Galaxy. Most regions where it is not detected in the Milky Way are associated with ongoing star formation but it is not seen in the spectra of local starburst galaxies. Until recently, the presence of the 2175Å feature in high redshift galaxies had not been considered.

The source of the 2175Å 'bump' has not been definitively identified. Current evidence suggests that polycyclic aromatic hydrocarbons (PAHs) are the molecules most likely to create the absoprtion feature (Tielens 2008). These molecules are dissociated by high energy photons such as those ubiquitous around hot young stars, consistent with the observation that the feature is associated with older stellar populations. Therefore, if the bluest UV galaxies at $z \sim 2.2$ are shutting down star formation, are more strongly clustered than their red neighbours, and harbour the carriers of the 2175Å absorption bump, they should also be more massive and older. It is possible to constrain these properties for individual objects through SED fitting. This work seeks to do just that by investigating the subsample of the KDF BX-selected objects with the bluest G-$\mathcal{R}$ colours. Here, G-$\mathcal{R} < 0.1$ is chosen as the definition of blue BX galaxies (hereafter bBX). Those with G-$\mathcal{R} > 0.1$ are referred to as red BX (rBX) objects.

1.4 Dust in High Redshift Galaxies

The presence of dust in galaxies alters the spectrum we expect to observe based on population synthesis models. As mentioned in Section 1.3, there is an interplay between stars and the dust that obscures them. Hot young stars emit radiation with sufficient energy to dissociate dust particles, preventing the formation of significant dust clouds. A galaxy needs time to come down from a period of active star formation so that its population of mellow, older stars dominates to permit the existence of dust. Noll et al. (2007b) propose hypothetical geometries that could permit fragile, PAH-containing dust to coexist with OB stars because its distribution with respect to regions of ongoing star formation would protect it from their UV photons. While these geometries are physically possible, they have never been observed. We proceed with the assumption that ubiquitous 2175Å dust in a galaxy corresponds to an old stellar population.

In a hospitable environment, dust grains are free to reprocess starlight. How they do so depends on the number, size, shape, composition and distribution of dust particles. Since they feel no compunction to arrange themselves uniformly in a galaxy, their effect can vary significantly between sight lines. In the Milky Way, dust attenuation along different lines of sight can be measured by observing absorption features imprinted by intervening dust clouds on the spectra of stars of known spectral types.

In the Milky Way, there is significant variation between observations in different directions, but the overall functional form of the dust attenuation spectrum is consistent (Fitzpatrick 1999). The 2175Å bump mentioned in Section 1.3, is visible in the absorption profiles of MW sight lines. The feature was first noted by Stecher (1969) in the UV spectra of ζ Persei and ϵ Persei. These UV observations were obtained using a multichannel scanner and 32-cm telescope mounted in a pointed Aerobee rocket. Near the peak of the rocket's flight the stars were observed sequentially. Subsequent observations showed that the bump can be well-described by a Lorentzian profile,

$$\left[(\tilde{\nu} - \tilde{\nu}_0)^2 + (\gamma_N/4\pi)^2 \right]^{-1}, \tag{1.2}$$

with $\tilde{\nu}_0 = 4.6\,\mu^{-1}$ and $\gamma_N = 6.28\,\mu^{-1}$ (Savage 1975) and that its central peak position is constant despite significant variability in its amplitude and width (Massa et al. 1982). As such, the bump is likely the result of a particular physical process occurring on a particular (currently unknown) type of dust grain. Current evidence points to polycyclic aromatic hydrocarbons (PAHs) as the responsible parties (Tielens 2008).

At high redshift, it is currently impossible to resolve components along different lines of sight in order to measure wavelength-dependent dust attenuation directly. It is possible to resolve structure in galaxies at $z \sim 2.2$ with instruments such as the Hubble Space Telescope and the Atacama Large Millimeter Array, but not to the degree possible for galaxies in the local universe. Calzetti et al. (2000) examined the energy balance between UV radiation absorbed by dust grains and the thermal IR radiation that they subsequently emit to calibrate the dust attenuation law for local starburst galaxies. Such a method could be applied to high redshift galaxies given spectroscopic observations of sufficient quality. However, to infer physical properties of dust in high redshift galaxies at present, we must make assumptions about the degree to which light is attenuated, generally by applying the dust reddening laws of nearby galaxies. The best-studied population of high redshift galaxies is the LBGs, simply because they are convenient to observe. Because of the amount of high energy photons spewing from these actively star-forming galaxies, the Lyman break is prominent. Around $z \sim 4$, it is redshifted to optical wavelengths, making it easily observable from the ground. Calzetti et al. (2000) included a discussion of observed similarities between local starburst galaxies and LBGs and suggested that the attenuation law they describe might be valid for this population.

Since then, the Calzetti dust law has become the convention for high redshift galaxies. Most analyses assume it by default and don't question its validity, e.g. Jaacks et al. (2012); Michalowski et al. (2012); Wake et al. (2011); Zhao et al. (2011); Finlator et al. (2010). This is not problematic in all cases (systems which are definitively known not to show a 2175Å feature or those with very little dust), but the importance of accurately correcting for dust attenuation cannot be overstated. Spectral indicators of star formation rate are all measured in the region of the 2175Å feature and excluding it from dust attenuation corrections can cause significant overestimations of SFR (Buat et al. 2011).

Improved dust correction has been shown to increase the efficacy of photometric redshift estimation (Ilbert et al. 2009; Kriek et al. 2011).

The goal of this thesis is to determine whether a dust law with or without a 2175Å feature best represents the bBX population and examine the implications of specific dust laws on physical properties of these systems. Chapter 2 introduces the data sets that are analyzed in Chapter 3. Chapter 4 examines the effect assuming an incorrect dust law on statistical clustering measurements and goes on to consider whether the 2175Å could be exploited as a photometric redshift indicator.

Chapter 2

Data

The most useful spectral feature for determining the age of a galaxy's stellar population is the Balmer/4000Å break because the difference between the continuum levels on either side of it increases as a stellar population gets older. The $UGRI$ data available in the KDF survey are not sufficient to capture the prominence of the break at $z \sim 2.2$ where its redshifted wavelength moves to ~ 13000Å: well into infrared regime. To capture the break in bBX objects, subfields of the KDF were observed with the Near InfraRed Imager and Spectrometer (NIRI; Hodapp et al. 2003) of Gemini North in 2010. Sections 2.2 and 2.3 describe reduction of these images and measurement of IR fluxes for objects in the KDF catalog. The images of objects in each of the previously analyzed $UGRI$ KDF and IR bands of the bBX objects in the NIRI subfields were stacked using the procedure described in Section 2.4. This produced an image of the average bBX object that is much deeper than any of the individual images from which it was made. The individual KDF bBX objects and the average stacked bBX object were analyzed with SED fitting to derive physical parameters of each galaxy as described in Sections 3.4 and 3.6. To verify the plausibility of the results found by SED fitting to the KDF bBX objects, photometric data for bBX objects with stronger IR detections than those of the objects in the KDF were obtained from Erb et al. (2006). This additional dataset is described in Section 2.5.

2.1 Gemini NIRI Observations

Three subfields of the KDF with large numbers of $UG\mathcal{R}$-selected BX objects (Equation 1.1) were selected for study in the infrared. Together, these fields provide a sample of 38 bBX-selected galaxies and 214 red BX-selected galaxies. Figure 2.1 shows the location of the subfields, designated 09.1, 09.2 and 09.3 in the KDF with the locations of member bBX-selected galaxies noted with red circles. Exposure times were chosen based on a simplistic but physically motivated scenario in which the bBX galaxies are either typical star-forming objects or passively evolving and massive. The IR observations were intended to constrain the masses of the bBX galaxies from the magnitudes of their Balmer breaks. Model galaxy SEDs were used to simulate the photometry of a typical star-forming galaxy and of a massive, dusty galaxy that may be shutting down star formation at $z \sim 2.2$. Both models had $\mathcal{R}_{AB} = 26.5$, the star forming model was assigned a mass of $2 \times 10^9 \, \mathrm{M}_\odot$, typical for high-z star-forming galaxies (Shapley et al. 2005) while the model shutting down its star formation had a mass of $2 \times 10^{10} \mathrm{M}_\odot$, prescribed by the hypothesis of Savoy et al. (2011). The massive, dusty models are brighter in the IR than the typical star-forming galaxies so the exposure times of the IR observations were set to achieve a depth between the two predicted magnitudes (H=23.9 and K=23.6 (AB)). For this simplistic binary model, failure to detect the bBX objects in the IR would suggest that they are typical star-forming galaxies while IR detections would suggest that they are indeed old and massive, consistent with the hypothesis. The NIRI Exposure Time Calculator was used to determine that total integration times of 1920s in K_s and 8280s in H were required to achieve 20% photometry assuming typical observing conditions.

The observations of the three KDF subfields were obtained in service mode with the Near InfraRed Imager and Spectrometer (NIRI) on Gemini North from February to April, 2010 with the broadband K_s ($\lambda_{\mathrm{central}} = 2.15\mu$m) and H ($\lambda_{\mathrm{central}} = 1.65\mu$m) filters. The total integration time for each field was divided into single exposures of 30 seconds. Table 2.1 summarizes the observations.

The field of view of each frame is 2' x 2' with a pixel scale of 0.1171 "/pix. The exposure pointing cycled through a nine point dither pattern of offsets. This serves to minimize the effect
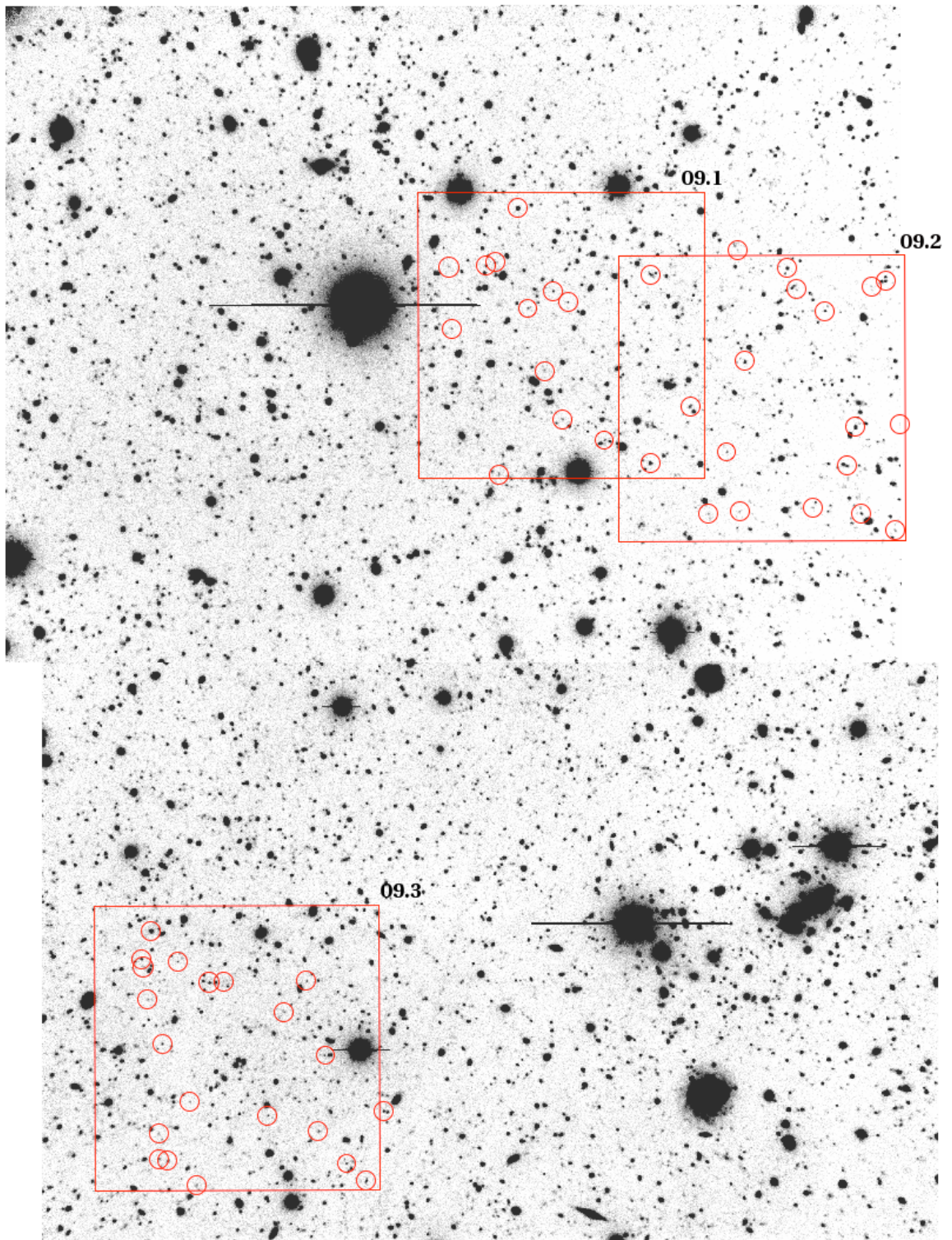
Figure 2.1: $\mathcal{R}$-band image of the 09A and 09B KDFs showing the locations of the 09.1, 09.2, and 09.3 subfields studied in the infrared with their member bBX galaxies marked in red. Each boxed subfield subtends $\sim 2'' \times 2''$.

Field	Filter	Date	N_{images}	Mean Airmass
09.1	K	2010-02-07	22	1.01
		2010-02-17	64	1.01
	H	2010-04-24	26	1.02
		2010-04-27	37	1.50
		2010-04-28	130	1.52
		2010-02-04	67	1.07
09.2	K	2010-02-13	64	1.18
	H	2010-04-28	120	1.02
		2010-04-28	121	1.22
		2010-05-06	43	1.15
09.3	K	2010-02-25	64	1.16
	H	2010-02-25	87	1.05
		2010-03-01	175	1.03

Table 2.1: Overview of Gemini NIRI H & K observations of 09.1, 09.2, and 09.3 KDF subfields.

of bright objects saturating portions of the detector, allows the sky brightness to be determined effectively during each exposure and minimizes the effects of bad pixels.

The calibration images needed to reduce the data were also obtained nightly. These included dark images to flag hot pixels, shutter flats and standard star observations. On each night of observations, standard IR stars whose absolute magnitudes are well known (Leggett et al. 2006) were observed in addition to the bBX objects to determine the photometric zeropoints. Each standard star observation consisted of 5 x 10s exposures using a 5-point dither pattern.

2.2 Image Reduction

Image reduction followed the usual IR processing steps of flatfielding, background subtraction, stacking with bad pixel masking and corrections for photometric zeropoints and airmass effects. This procedure is explained in detail below.

The IR data were obtained from the Gemini Science pipeline and required processing before photometry could be performed. Figure 2.2 shows an example of a raw 30 second exposure. Data
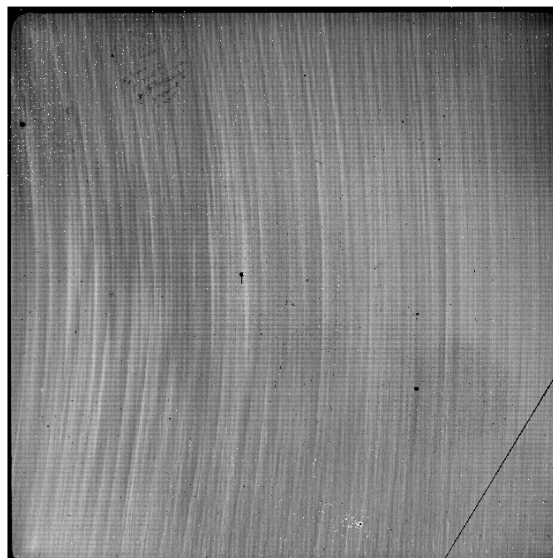
Figure 2.2: Sample raw 30s *H*-band exposure of the 09.1 KDF subfield. The diagonal black line in the bottom right corner is the result of dead pixels on the detector. The dither pattern used in the observations serves to eliminate the effects of pixels like these by having a given point on the sky arrive at different points on the detector in different exposures. In the final reduced images, no such effects appear.

reduction was performed with IRAF [1] using a combination of native tasks and tasks from the Gemini IRAF package.

For each night of observations, a bad pixel mask (BPM) was derived from short dark images (with exposure times of ∼0.01s), taken with no light falling on the detector. The Gemini IRAF task `niflat` examines these images, flagging hot pixels which record detections when no signal falls on them and dead pixels which have no response to signal. These pixels are ignored in the subsequent image analysis by means of the BPM. In addition to these egregiously malfunctioning pixels, it is important to flag pixels which exhibit anomalous behaviour that is not apparent in the short dark images. Pixels which saturate over the exposure time of the science images must also be excluded to obtain accurate photometry. Thirty second dark images were used to flag these pixels, by examining the distribution of count rates registered by individual pixels using the task `imexamine` and then

---

[1]IRAF is distributed by the National Optical Astronomy Observatories, which are operated by the Association of Universities for Research in Astronomy, Inc., under cooperative agreement with the National Science Foundation.

identifying those with count rates in the tail of the distribution with `imreplace`. These pixels were added to the `niflat` bad pixel masks.

The `niflat` task also creates master flat field images. To derive a flat field, 2 sets of images are taken with the Gemini calibration unit GCAL. One set of images is taken with the instrument shutter open and the detector illuminated uniformly by a calibration lamp. A second image set is obtained with the shutter closed to measure dark current and thermal background from optical components in the instrument. `niflat` combines these sets of images separately and subtracts the thermal background from the combined lamp image. The result is normalized to create a map of the detector's response to a uniform signal known as a flatfield.

Both the light from distant objects and the brightness of the sky on Earth contribute to the signal that arrives at the detector. This sky brightness must be measured and subtracted from the science images. Atmospheric effects cause the IR background to vary on very short time scales compared to visible wavelengths. To take this into account, the sky brightness level for each science exposure was found using the image itself combined with the 4 previous and the 4 subsequent images in the run. Each sky image thus samples the mean background sky over 4.5 minutes (except for images from the beginning and end of each run) and uses one position from each point in the 9 point dither pattern. The Gemini task `nisky` was used to median combine each group of 9 images. This task first creates a simple median sky image from the set of images which it uses to reduce the nine input images in a first pass. Bright regions are then identified in the input images to create an object mask for each image. The final sky image is then produced by averaging the first-pass reduced input images with the object masks applied. This should prevent bright regions from skewing the average count rate at any location upward. However, the afterglow from bright foreground stars in the field can create artifacts in the images by heating the pixels they illuminate. These pixels then emit thermal radiation which registers as signal falling on the detector in the next image. In the course of the image reduction procedure it was found that many of these afterglow effects were not eliminated by `nisky`. An average sigma clipping algorithm, which eliminates pixels with counts 1σ above or below the average for that pixel in all frames, was applied during the creation of the sky
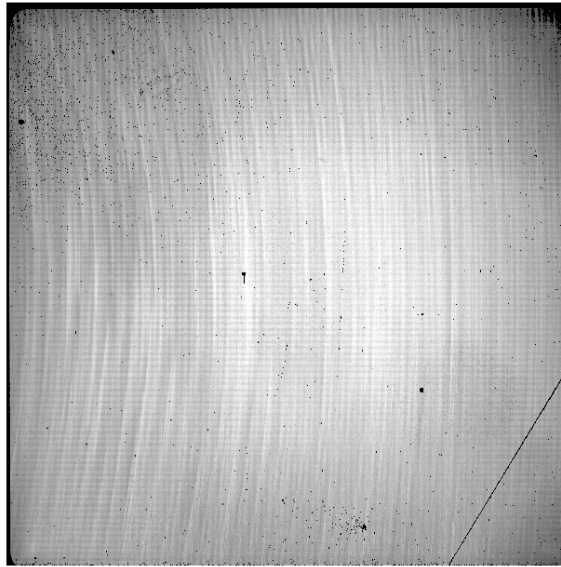
Figure 2.3: Sky image for an 09.1 frame generated by combining nine 30s exposures, one at each point in the dither pattern and taken over a period of 4.5 minutes. Bright objects are masked in each exposure before stacking to obtain an image which accounts for the brightness of the sky, and is not skewed by astronomical objects.

images. This reduced the problem to a negligible level.

Once the detrending frames were generated, the Gemini task `nireduce` was used to apply them to the science images. This task subtracts the background sky level from each pixel and divides it by the value of the normalized flat field. The amount of atmospheric extinction scales linearly with airmass which varied significantly over the course of each observing run. All images were scaled to an equivalent airmass of 1 using the values measured by Leggett et al. (2006) for the IR extinction per airmass and the airmass measurement of each observation, noted in the FITS headers. They were then stacked with dither offsets and using BPMs to mask out bad pixels.

This image reduction procedure was first performed on the standard star images. The instrumental magnitudes of standard stars on each night were measured from the reduced images using the radial profile tool of the `imexamine` task. Vega magnitudes for the standard stars were obtained from Leggett et al. (2006) and converted to AB magnitudes using the infrared Vega-AB magnitude conversion described by Tokunaga & Vacca (2005). The difference between the known

AB magnitude of a standard star and its instrumental magnitude gives the nightly photometric zeropoint.

The images of the KDF subfields were then reduced as described above and then corrected to the photometric zeropoint and scaled to an equivalent exposure time of 1s. This resulted in a set of images of each field taken on multiple nights, but corrected to the same exposure time, zeropoint and airmass. These reduced science images for each field were combined with `imcombine`. Some artifacts resulting from pixel saturation and afterglow effects of the dither pattern were still present. To reduce this effect to levels that would not impact photometry, a min/max rejection method was used in stacking the frames. The 5% highest and lowest pixel values were excluded from the brightness calculated at each location. Figure 2.4 shows the final stacked image for the 09.2 field in the H-band.

As previously mentioned, the Gemini observations were designed to obtain 20% photometry for objects with H=23.9 and K_s=23.6 (AB) assuming typical observing conditions. The reduction procedure described above resulted in images with 1σ limiting magnitudes of ~ 23.9 and ~ 23.3 in H and K_s respectively (the calculation of photometric detection limits is described in Section 2.3). These depths were shallower than expected and as such, the majority of BX objects (both red and blue) were not detected.

2.3 Photometry

The goal of the observations described in Section 2.2 was to measure the IR fluxes of BX objects in the subfields and combine these data with the $UG\mathcal{R}I$ photometry from previous KDF analyses so that their SEDs could be fit more robustly. As such, associating the objects in the KDF catalog with their IR image counterparts was a crucial part of this analysis. Unfortunately, matching the objects' positions was complicated by the fact that none of the bBX objects and only a handful of rBX objects were detected in either infrared band. To sidestep this issue, the transformation from optical coordinates to the infrared ones was computed using the positions of bright foreground objects that
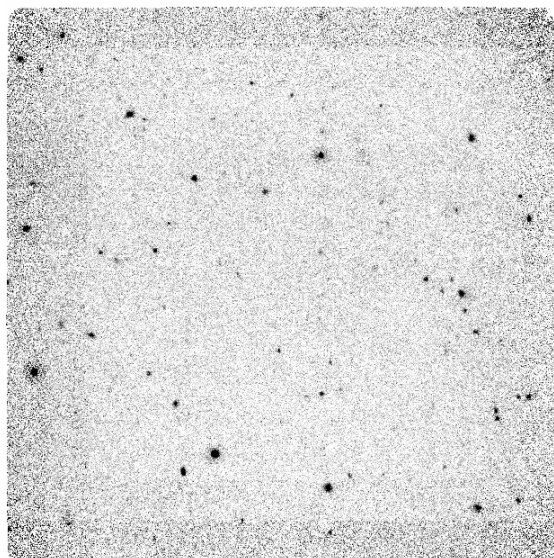
Figure 2.4: Reduced *H*-band image of 09.2 field. The increase in noise at each edge reflects the fact that these regions are covered by fewer positions in the 9 point dither pattern.

could be readily correlated in the IR and *UGRI* images. This made inference of the bBX objects' positions possible so that blind photometry could be performed at the correct locations.

To determine the transformation between the optical and IR coordinate systems, objects visible in both the *R* (the deepest of the KDF observations) and IR images were marked manually in DS9[2] using the *autocentroid* feature which assumes a Gaussian profile for selected objects and adjusts the position of a marked location to the centroid it calculates from surrounding pixel values. The RA and DEC of each object in the $\mathcal{R}$-band images selected and matched in the IR were converted to equivalent positions in image coordinates for the IR images using the reference coordinates of the telescope pointing from the FITS headers. The two sets of xy image positions for common objects were analyzed using the IRAF task `geomap` to compute the best fit transformation, allowing the inclusion of shifts in x and y, scaling, and rotation. The transformation prescribed by `geomap` was then applied to the positions of the BX objects from the KDF survey using the `geoxytran` task to find the positions of the KDF objects in the IR images. This procedure was repeated for each field and filter.

---

[2]This research has made use of SAOImage DS9, developed by Smithsonian Astrophysical Observatory

SExtractor version 2.5.0 (Bertin & Arnouts 1996) was used to perform aperture photometry on the IR images. When fluxes for a specific population (in this case, the KDF BX objects) are to be measured, SExtractor identifies all objects in the field and performs photometry. Then the coordinates of the objects of interest may be specified in a cross-identification catalog and are used to reselect the relevant objects in the second image. This feature makes SExtractor extremely useful for identifying objects in crowded fields and separating flux contributions from overlapping objects, but for non-detected objects, as is the case here, this makes it impossible to simply perform photometry at the required locations. To trick SExtractor into making measurements at the locations determined form the R-band-to-IR transformation computed in IRAF, SExtractor's *double image mode* was used. This mode allows one image to be used to identify the locations of objects and then uses those locations to perform photometry in a second image. Since only the BX objects were of interest to this analysis, artificial images were generated with point sources at the transformed positions of the BX objects. These images were used in *double image mode* for object location and then aperture photometry was performed on the IR images. Consistent with the prior KDF analysis, circular apertures of diameter 2" were used.

When SExtractor was used to determine the BX object fluxes, we found quantities in agreement with those found manually with the IRAF task `imexamine` but the SExtractor flux uncertainties were nonsensically (by as much as 20 dex) large due to a problem in the program. Local background variations at the position of the objects were thus computed separately (but in the same way that SExtractor should). Object masks were created for the H and K images of each field with SExtractor by generating segmentation-type *check images*, which display patches corresponding to the pixels of each object. The check-images were smoothed using the IRAF task `gauss` to pad the detection region of each bright object and ensure complete masking. Pixel values were converted to integer values using `imreplace` to conform to the pixel-list file format required for masks. The masks were applied to the stacked images and the `imstat` task was used to calculate pixel statistics for rectangular regions of $\sim 150 \times 150$ pixels[3] at the location of each object, ignoring those pixels

---

[3]The 150×150 pix regions used to calculate pixel statistics correspond to an area of $\sim 147 \times 147$ kpc at $z = 2.2$

flagged in the object masks. The variation in each region was used to compute the local 1σ limiting magnitude at the position of each target.

When multiwavelength observations of an object are combined to constrain its SED with aperture photometry it is generally important to homogenize the point spread functions of images in each waveband to ensure light from the object is smoothed into and out of the aperture uniformly. This is done by smoothing all images so that they all have PSFs corresponding to that with the poorest resolution. For these IR images, this step was deemed unnecessary because of the very low detection rate. The photometric data for the 36 bBX objects considered in this analysis are listed in Table 2.2

2.4   Stacking Analysis

The IR observations were intended to measure the strength of the Balmer/4000Å break in the bBX population to constrain the age of the population. However, the vast majority of the KDF BX objects were detected in neither of the IR bands so it was only possible to place limits on their H and K magnitudes. Difficulty obtaining sufficiently deep data to detect targets is a common problem in high-redshift astronomy because typical objects are so faint. One method for increasing the depth of observations of a given population without resorting to unfeasibly long exposure times is to stack images of objects known to have similar properties, e.g. Bourne et al. (2012), Guaita et al. (2011), Magnelli et al. (2009). By taking the mean pixel value of the region around each object, the background noise is reduced. This stacking relies on the assumption that all included objects are representative of the population and that their properties are normally distributed. This assumption is not ideal because the objects in the sample are distributed over a range of redshifts and have varying intrinsic properties whose distributions are generally not known. In some cases, the non-normality of a property is evident, such as the distribution of galaxy luminosities. The form of the luminosity function at $z \sim 2.2$ (Sawicki & Thompson 2006a) is clearly not a normal distribution, however this

---

in the adopted cosmology: $(\Omega_M, \Omega_\Lambda, H_0) = (0.3, 0.7, 70\,\mathrm{km\,s^{-1}\,Mpc^{-1}})$. Where Ω_M is the matter density parameter, Ω_Λ is the density parameter for the cosmological constant and H_0 is the Hubble constant.

KDF#	U_n	σ_U	$U_{n\,lim}$	G	σ_G	G_{lim}	$\mathcal{R}$	$\sigma_\mathcal{R}$	$\mathcal{R}_{lim}$	I	σ_I	I_{lim}	H	σ_H	H_{lim}	K_S	σ_{K_S}	$K_{S\,lim}$
499	25.52	0.03	29.80	25.08	0.02	29.85	25.10	0.03	29.09	25.08	0.05	28.58	24.79	0.35	23.73	24.12	0.28	23.28
550	26.33	0.09	29.88	25.84	0.05	29.90	25.92	0.11	29.14	25.57	0.13	28.61	25.01	0.63	23.79	25.00	0.96	23.33
591	26.38	0.07	29.87	25.78	0.03	29.89	25.74	0.07	29.12	25.73	0.10	28.60	25.08	0.64	23.47	24.67	0.67	23.01
592	26.97	0.09	29.88	26.57	0.05	29.90	26.54	0.09	29.13	26.01	0.10	28.60	24.97	0.39	23.57	24.10	0.28	23.07
600	25.73	0.04	29.82	25.50	0.02	29.88	25.47	0.05	29.11	25.55	0.08	28.60	25.27	0.57	23.69	23.97	0.27	23.22
717	26.44	0.06	29.86	26.15	0.04	29.90	26.24	0.08	29.13	25.83	0.09	28.60	25.41	0.52	23.83	24.59	0.38	23.35
749	25.85	0.04	29.84	25.53	0.03	29.88	25.49	0.05	29.11	25.32	0.07	28.59	26.45	2.67	23.38	24.92	1.19	22.74
860	26.95	0.15	29.90	26.13	0.06	29.90	26.12	0.12	29.14	25.84	0.14	28.60	24.41	0.31	23.80	24.02	0.33	23.33
1183	26.50	0.07	29.87	26.14	0.04	29.89	26.14	0.08	29.13	25.81	0.10	28.60	24.76	0.30	23.82	24.12	0.26	23.32
1293	26.20	0.05	29.85	25.85	0.03	29.89	25.81	0.06	29.12	26.00	0.12	28.60	24.99	0.38	23.82	24.22	0.29	23.32
1711	26.82	0.07	30.24	26.42	0.04	30.11	26.45	0.07	29.42	26.21	0.09	28.90	23.81	0.19	23.29	23.74	0.24	23.02
1713	27.55	0.13	30.29	27.13	0.07	30.09	27.15	0.13	29.38	26.95	0.18	28.86	24.54	0.38	23.23	24.08	0.30	23.02
1768	24.25	0.02	29.63	24.06	0.01	29.77	24.13	0.02	29.16	23.91	0.02	28.68	23.62	0.18	23.68	23.48	0.21	23.37
2016	24.80	0.03	29.87	24.55	0.02	29.88	24.58	0.03	29.22	24.56	0.05	28.73	23.65	0.22	23.66	23.26	0.20	23.35
2027	26.25	0.07	30.12	25.92	0.04	29.98	25.90	0.07	29.28	25.30	0.07	28.75	25.74	1.37	23.45	23.56	0.22	23.27
2074	26.84	0.09	30.17	26.61	0.06	30.00	26.65	0.14	29.30	26.05	0.10	28.76	26.13	1.59	23.47	25.00	0.74	23.16
2120	25.19	0.03	29.90	24.78	0.01	29.87	24.74	0.02	29.21	24.62	0.04	28.72	25.19	0.62	23.74	24.55	0.46	23.43
2161	28.70	0.32	30.27	28.07	0.15	30.02	28.04	0.35	29.31	26.96	0.16	28.77	25.86	0.64	23.72	25.30	0.51	23.41
2292	27.93	0.18	30.24	27.38	0.09	30.01	27.39	0.16	29.30	27.30	0.25	28.78	27.43	2.93	23.74	26.72	2.09	23.40
2323	26.51	0.07	30.14	26.05	0.04	29.98	26.11	0.07	29.28	26.21	0.15	28.77	22.72	0.06	23.66	22.95	0.10	23.35
2364	26.87	0.09	30.17	26.54	0.05	30.00	26.55	0.10	29.29	26.89	0.27	28.78	23.81	0.21	23.31	24.26	0.29	23.39
2384	24.67	0.02	29.70	24.21	0.01	29.75	24.18	0.01	29.13	24.12	0.02	28.68	23.52	0.17	23.33	26.13	1.80	23.39
2449	27.48	0.12	30.20	27.18	0.08	30.01	27.25	0.19	29.30	26.53	0.13	28.77	25.67	0.84	23.40	24.48	0.37	23.09
2505	27.21	0.13	30.21	26.36	0.05	29.98	26.39	0.08	29.28	26.67	0.19	28.77	24.37	0.31	23.42	24.75	0.59	23.11
2519	27.42	0.12	30.20	27.24	0.08	30.01	27.32	0.16	29.30	28.45	0.99	28.78	25.70	0.77	23.58	24.76	0.55	23.00
2534	25.96	0.04	30.03	25.78	0.03	29.95	25.81	0.05	29.26	25.69	0.09	28.76	25.27	0.57	23.76	23.49	0.15	23.41
2593	26.57	0.07	30.13	26.21	0.04	29.98	26.18	0.08	29.28	26.04	0.11	28.76	25.06	0.47	23.72	24.41	0.33	23.44
2676	27.43	0.16	30.23	26.81	0.07	30.01	26.77	0.12	29.29	27.04	0.29	28.78	98.74	99.00	23.61	22.23	0.05	23.39
2730	27.96	0.19	30.24	27.46	0.10	30.02	27.42	0.20	29.30	27.30	0.31	28.78	25.44	0.73	23.47	23.42	0.19	22.82
2929	27.05	0.09	30.17	26.52	0.05	29.99	26.55	0.08	29.28	26.88	0.20	28.77	24.59	0.27	23.63	25.70	0.87	23.46
2941	23.83	0.01	29.34	23.65	0.01	29.60	23.72	0.01	29.04	23.63	0.01	28.62	24.98	0.57	23.44	24.04	0.25	23.41
3007	26.17	0.05	30.08	25.81	0.03	29.96	25.77	0.06	29.27	25.17	0.05	28.74	24.44	0.34	23.53	26.35	2.06	23.47
3154	27.80	0.18	30.24	27.24	0.09	30.01	27.33	0.19	29.30	27.09	0.27	28.78	24.02	0.16	23.63	24.13	0.20	23.52
3411	26.48	0.06	30.11	25.81	0.03	29.95	25.84	0.05	29.26	25.72	0.07	28.75	98.85	99.00	23.74	26.19	1.47	23.50
3490	26.76	0.07	30.13	26.47	0.04	29.99	26.51	0.08	29.29	26.46	0.14	28.77	20.44	0.01	23.70	24.20	0.29	23.18
3504	26.42	0.06	30.11	26.10	0.04	29.97	26.15	0.07	29.28	26.22	0.13	28.77	24.21	0.60	22.60	23.84	0.26	23.18

Table 2.2: $UG\mathcal{R}IHK$ photometric magnitudes for KDF bBX objects with IR observations. Column 1 gives the KDF catalog ID number of each object, columns 2, 5, 8, 11, 14, and 17 give the AB magnitude of objects in each filter, columns 3, 6, 9, 12, 15, 18 give the associated 1σ uncertainties, and columns 4, 7, 10, 13, 16, and 19 give the 1σ detection limit at the position of each object as determined by sky level fluctuations in 150×150 pixel regions centered on each object. Magnitudes and uncertainties > 98 indicate non-detections.

stacking procedure provides a reasonable first approximation of prototypical bBX object.

Deeper data for the average bBX and rBX object in the sample were obtained by stacking the individual objects in each filter. For each bBX and rBX-selected object, a 23.5"x23.5" image centered on it was cropped from the larger KDF field. For the Keck data, object positions were taken from the KDF catalogue and for the IR data the positions calculated by the method described in Section 2.3 were used. For each filter, the cropped images were stacked using the IRAF task `imcombine` weighting detections and non-detections equally. In the stack, each object image was rotated $90°$ relative to the previous frame as a precautionary measure to compensate for any large scale gradient background effects. Figures 2.5 and 2.6 show the resultant images in each filter.

With the increased signal strength in all filters the difference between point spread function widths in each waveband becomes important. The PSF width of each data set was measured using the IRAF task `psfmeasure`. The Keck *G* data had the poorest resolution with a PSF FWHM of 1.549". Gaussian smoothing was applied to the *URIHK* data with the IRAF task `gauss` so that all images had the same PSF width. Photometry was then performed as described in Section 2.3. Each stack was made up of object frames cropped from different KDF images, each of which had a different photometric zeropoint. To determine the zeropoint of the stacked image, the zeropoint of each KDF image was first converted to a flux. The average of these values, weighted by the number of BX-selected objects included in each stack, was calculated, then converted back to a magnitude. This method gave zeropoints for the bBX and rBX stacks which were applied to both sets of photometric measurements. Table 2.3 presents a summary of the results.

The effective increase in depth provided by the stacking procedure yields H and K detections for the average rBX object and better constrains the average bBX object's IR photometry. A weak signal is visible at the center of both the *H* and *K* bBX stacks, however it is not statistically significant at the 1σ confidence level used in this analysis. Having averaged over many sight lines, it is reasonable to assume that the effects of stochastic intergalactic attenuation have been reduced so that the average U-band photometry is more reliable for the stacks than for individual objects and can be used in SED fitting.
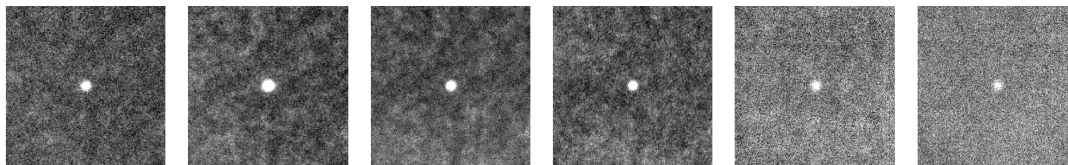
Figure 2.5: Average rBX object images in *UGRIHK* wavebands generated from 177 KDF objects.
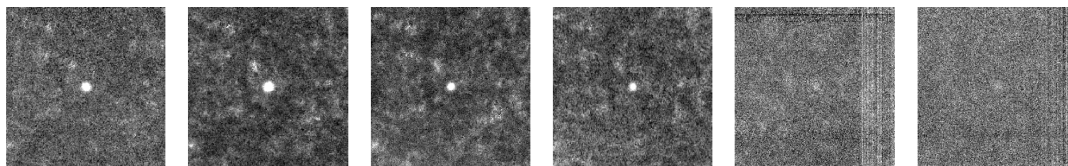

Figure 2.6: Average rBX object images in *UGRIHK* wavebands generated from 36 KDF objects.

The photometry in Table 2.3 is somewhat deceptive in that the stated uncertainties only include the contribution from background noise. In reality, the photometric uncertainty depends both on background noise fluctuations and on the inhomogeneity of the sample which includes variability in both luminosity and redshift of the objects in the sample. To estimate the contribution of sample inhomogeneity, a jackknife analysis was performed and found $\sigma_m \sim 0.6$, dwarfing the background uncertainty contribution. The true uncertainty in photometry is the quadratic sum of σ_{inhom} and σ_{back}. However, when SED fitting was performed using these values, the results showed that the errorbars were grossly overestimated. This is because the stacking analysis relies on the assumption that the brightness distribution of the sample is normal. This is doubly wrong in that the objects are also distributed over a range of redshifts (increasing their range of observed brightnesses) and a range of luminosities (Sawicki & Thompson 2006a), neither of which is Gaussian. To measure model parameters with SEDfitting, we want photometric uncertainties to reflect the distribution of intrinsic luminosities but not that of redshifts (perturbing the galaxies redshift will cause a systematic shift in its photometry at all wavelengths). To determine the uncertainty necessary to reflect the underlying intrinsic scatter in the data, the average rBX object was fit with various softening parameter values (additional photometric uncertainty included in the fitting procedure). Assuming that the best fit model is the 'right' one, the expected value of χ^2 is the number of degrees of freedom, in this case 3. A magnitude softening of 0.15 was found to yield this result and was added to the background

	rBX			bBX		
$N_{objects}$	177			36		
	$\mathbf{m}_{AB}$	σ_m	$\mathbf{m}_{lim}$	$\mathbf{m}_{AB}$	σ_m	$\mathbf{m}_{lim}$
U	26.72	0.02	29.13	26.21	0.02	28.38
G	25.86	0.01	29.12	25.76	0.01	28.45
R	25.56	0.01	28.32	25.97	0.03	27.63
I	25.46	0.01	27.89	25.75	0.03	27.12
H	25.00	0.04	25.90	25.57	0.18	25.03
K	24.63	0.04	25.61	24.85	0.12	24.82

Table 2.3: Photometry of average rBX and bBX object stacks. Photometric uncertainties measure background noise fluctuations only. The distribution of rest frame properties is not considered.

uncertainty in all 6 filters used in the SED fitting described in section 3.6.

2.5 Erb et al. (2006) Data

In considering the individual KDF bBX objects, the main source of uncertainty in constraining their properties was the unreliable U band data, stochastically affected by IGM attenuation. An independent confirmation of the redshifts would verify the results. To see whether the parameters found in the analysis of the bBX photometry were reasonable, bBX objects for which both similar photometric data and spectroscopically measured redshifts were available was analyzed. These data were obtained from the sample studied by Erb et al. (2006). Erb et al. (2006) fit models to BX objects whose redshifts had been determined spectroscopically from $H\alpha$ measurements. Nine BX objects included in their analysis have G-R colours which satisfy the bBX criteria defined in Chapter 1. The photometric data for these objects are summarized in Table 2.4. Corresponding uncertainties were not presented with these data. For the purpose of the SED fitting described in Section 3.5, errorbars were assigned to the Erb et al. (2006) data similar to those found for the KDF photometry.

Identifier	$z_{H\alpha}$	U_n	G	$\mathcal{R}$	J	K_s
HDF-BX1376	2.4294	25.19	24.49	24.48	24.06	23.98
HDF-BMZ1156	2.2151	24.40	24.61	24.62	22.95	22.18
Q1623-BX432	2.1817	25.21	24.68	24.58	24.15	23.33
Q2343-BM133	1.4774	22.78	22.59	22.59	22.07	22.35
Q2343-BX163	2.1213	24.77	24.06	24.07	23.26	23.23
Q2343-BX418	2.3052	24.31	23.94	23.99	24.55	23.73
Q2343-BX599	2.0116	24.41	23.60	23.50	22.50	22.25
Q2343-BX660	2.1735	24.72	24.27	24.36	24.15	22.83
Q2343-MD80	2.0138	26.23	24.90	24.81	23.44	23.23

Table 2.4: $UGRIJK_s$ photometry for bBX objects from Erb et al. (2006). The $H\alpha$ redshift of Q2343-BM133, $z_{H\alpha} = 1.4774$, makes it fall outside the expected redshift range of BX galaxies. It is not excluded from the analysis because it nevertheless satisfies the selection criteria and the uncertainty in the spectroscopically determined redshift is unknown.

Chapter 3

Spectral Energy Distributions

Colour-colour selection methods for high redshift galaxies like those mentioned in Section 1.1 are useful for selecting large samples of objects but they are of little use when it comes to pinpointing the underlying characteristics of an object because of the few data points considered. When more complete photometric data for an object are available, its properties can be further constrained by comparison with galaxies whose parameters are known. The analysis used in this work employs the program SEDfit (Sawicki 2012) to compare object photometry to a set of theoretical models. The preceding chapter introduced sets of photometric data for three types of objects: the bBX objects in the KDF subfields observed in the infrared, the photometry from deeper stacked images (for both the bBX and rBX-selected objects), and the photometry and $H\alpha$ spectroscopic redshifts of bBX objects obtained from the sample of Erb et al. (2006). The present chapter describes the application of an SED fitting procedure to each of the data sets. The goal of this analysis was to compare the parameters of the best fitting models with those consistent with the hypothesis of bBX objects being dusty galaxies shutting down star formation.

3.1 Modeling Galaxy SEDs

The first step in finding a model that describes photometric data is to generate a set of model galaxy spectra to which observations can be compared. In this analysis, desired physical parameters include each galaxy's redshift, mass, age, star formation rate, and dust content. This section describes the process of generating a grid of model galaxy spectra that span this parameter space.

3.1.1 Population Synthesis Modeling

To simulate data for a high redshift galaxy as it would be observed from Earth, it is first necessary to model its rest frame spectrum. Theoretical rest frame SEDs can be generated using the method of isochrone synthesis modeling, described by Bruzual & Charlot (2003). The spectrum of a galaxy is first approximated by the sum of the spectra of all the stars it contains. Since stellar evolution is quite well understood, it is possible to follow the evolution of a galaxy spectrum by considering the changing spectra of its constituent stars. The GALAXEV code of Bruzual & Charlot (2003) sets up an initial stellar population from an initial mass function and metallicity parameter. The code follows the time evolution of the system with a library of stellar evolution data, adding new stars according to a specified time-dependent star formation rate. The obscuring effects of dust within the galaxy itself, and gas between the galaxy and observer can be included as attenuation functions which modify the stellar spectrum.

3.1.2 Dust in High Redshift Galaxies

Not all galaxies exhibit the 2175Å feature- the attenuation spectrum of a galaxy depends on the unique dust population residing in its ISM. This spectrum can be measured by looking for UV absorption features and IR continuum emission in the spectra of objects whose intrinsic SEDs are known. With measurements of this spectrum along many lines of sight (as in Figure **??**) it is possible to empirically derive the functional form of its average dust extinction. This gives a dust law which can be applied to observations to correct for wavelength-dependent dust attenuation. These dust

laws are conventionally expressed in the form

$$f_{obs}(\lambda) = f_{int}(\lambda)10^{-0.4A_\lambda} \qquad (3.1)$$

where f_{obs} is the observed flux and f_{int} is the intrinsic flux. The extinction at a given wavelength depends on the colour excess $E(B-V)$ and on the reddening curve $k(\lambda)$:

$$A_\lambda = k(\lambda)E(B-V) = \frac{k(\lambda)}{R_V} \qquad (3.2)$$

where R_V is a constant which varies between dust laws. The dust attenuation spectra of the LMC (Fitzpatrick 1986) and MW (Fitzpatrick 1999) include 2175Å features, the underlying continua of the two are different so the two laws have different shapes. The dust law for local star-forming galaxies of Calzetti et al. (2000) does not exhibit the absorption feature.

3.1.3   IGM Attenuation

A difficult complication in simulating the effects of redshifting the population synthesis models of rest-frame galaxy spectra is the stochastic effect of intergalactic gas. This effect is redshift dependent (the more distant an object, the more gas clouds its light encounters) but the variation between different lines of sight is significant. Intergalactic attenuation laws can be expressed in the form

$$L_\nu''(\lambda) = L_\nu'(\lambda) \cdot e^{-\tau_{\text{eff}}(\lambda,z)} \qquad (3.3)$$

where L'' is the IGM-attenuated SED and L' is the dust-attenuated SED. τ_{eff} is the effective optical depth which depends on the redshift of the source. The column density of absorbing material increases with distance between the source and observer and the absorption wavelengths are affected by the cosmological redshifts of the absorbers . In this analysis, the prescription of Madau (1995), which describes the IGM attenuation along an average line of sight, is used. At z~1.6 the Lyman

limit (at rest frame 912Å) moves into the U filter. Since we seek to determine each object's redshift photometrically, the limit's precise location in wavelength space is not known: the situation is no longer as simple as it is for higher redshifts where a non-detection in U is indicative of data straddling the Lyman limit. This fact combined with the significant variability (increasing with redshift) of IGM attenuation make the U-band photometry for the objects in our redshift range of interest unhelpful. As such, it is excluded from fits to individual objects.

3.2   SEDfit

Colour-colour selection methods for high redshift galaxies like those described in Section 1.1 can only go so far in telling us about an object's intrinsic properties. Using a maximum-likelihood approach to compare photometric data for an object to synthetic data of model objects with known parameters takes the investigation further. SEDfit is a software package for fitting model SEDs to photometry (Sawicki 2012). It is unique in its ability to account for non-detections and upper limits which arise frequently in high redshift astronomy. The fitting procedure occurs in two steps: generating a grid of models and determining which model best fits the data.

To produce a model grid that includes redshift as a parameter, SEDfit begins with rest frame SEDs (e.g. those generated by the GALAXEV code of Bruzual & Charlot (2003)). To produce rest frame SEDs, star formation history, IMF, metallicity and dust content must be specified. These parameters determine the time evolution of a galaxy spectrum which can be extracted at various ages. SEDfit then modifies the rest frame spectra to create a grid of model spectra as they would appear redshifted in a specified cosmology. The redshifting procedure accounts for interstellar dust attenuation, cosmological dimming, and redshift-dependent attenuation by intergalactic clouds along the line of sight in addition to wavelength shifting. The redshifted models are then convolved with the transmission functions of the filters used to obtain photometric data to produce a grid of model magnitudes. SEDfit can then compare the model magnitudes and photometric data to determine the best-fitting model using a maximum likelihood test, minimizing

$$\chi^2 = \sum_i \left(\frac{f_{d,i} - s f_{m,i}}{\sigma_i} \right)^2 \tag{3.4}$$

where $f_{m,i}$ if the model flux density through the ith filter and $f_{d,i}$ is the corresponding observed flux density with uncertainty σ_i. The normalization, s, is determined analytically.

When non-detections are present in the data, the maximum likelihood statistic is modified to include these faint limits, enumerated j:

$$\chi^2 = \sum_i \left(\frac{f_{d,i} - s f_{m,i}}{\sigma_i} \right)^2 - 2 \sum_j \ln \int exp \left[-\frac{1}{2} \left(\frac{f - s f_{m,j}}{\sigma_j} \right)^2 \right] df \tag{3.5}$$

where $f_{lim,j}$ is the 1σ flux detection limit of the jth filter. When an object is detected in all bandpasses, the flux scaling, s, can be determined analytically but when non-detections are present, Equation 3.5 must be integrated numerically, greatly increasing the computational cost of fitting.

3.3 Models

The model SEDs considered in this analysis sampled a variety of star formation histories and dust laws. The GALAXEV program of Bruzual & Charlot (2003) was used to generate isochrone synthesis models with a metallicity of $0.4Z_\odot$ and a Salpeter IMF Salpeter (1955). The models include time-dependent star formation of the form SFR$\propto e^{(-t/\tau)}$ for values of $\tau = -1, 0.1, 1, 3$ as well as constant star formation ($\tau = 0$) and a single, instantaneous burst of star formation ($\tau = \infty$). High redshift star-forming galaxies are generally modeled with constant star formation while dusty "red and dead" galaxies are modeled with a single stellar population. The set of star formation histories considered in this analysis span the plausible range of star formation histories and encompass the models typically used in similar analyses. For each of the star formation histories, SEDs were extracted at 220 ages ranging from 0.1 Myr to the age of the universe at redshift 2.2

($\sim 10^{9.6}$ years). SEDfit was used on these rest-frame models to apply average line of sight Madau (1995) IGM attenuation, each of the dust attenuation laws described in Section 1.4 with values of $E(B - V)$ ranging from 0.0 to 1.0 at intervals $\Delta E(B - V) = 0.01$, and redshifting from $z = 0$ to $z = 5$ at intervals $\Delta z = 0.01$. The resulting spectra were convolved with the appropriate $U_n G \mathcal{R} I H K_S$ filter transmission curves, giving AB magnitudes for comparison with the KDF photometry. The SEDfit model grid comprises spectra of galaxies with an initial mass $M_{t=0} = 1 M_\odot$ (so that models with non-zero star formation will have higher mass at subsequent ages) which are compared to data to select the best-fitting model and normalization which scales the model galaxy mass to the mass that best describes the data. Thus the selected model determines the best-fitting redshift, reddening and age, while the SFR and stellar mass are properties of the normalization. This method for determining physical parameters suffers from degeneracies between the spectra resulting from varying intrinsic galaxy parameters relative to the uncertainties of photometric data.

3.3.1 A Note on Smoothing

Plots comparing photometric data with model spectra can be somewhat misleading. Photometry ultimately results from the convolution of the underlying spectrum and the transmission curve of the filter (FTC) used at each wavelength. Plotting a single point at the effective wavelength (generally defined as the wavelength that bisects the area under the transmission curve) of the filter can make a fit look deceptively poor if the width of the filter is large compared to the scale over which the spectrum changes. This can obviously be problematic when strong lines are present in models, but could be here as well. In the bBX object fits, the R band filter's central wavelength is coincident with the minimum of the 2175Å feature. For narrow absorption features, if the object's flux is higher at wavelengths near the edges of the filter than at its center, photometry may look questionably high compared to the model, as is the case with the R band filter used here for objects with particular combinations of dust content and redshift. While programs like SEDfit are not hindered by this effect (because the data and models are convolved with the same transmission functions), inspecting the best fits by eye can be unnerving if the width of filters is not considered. To illustrate the degree
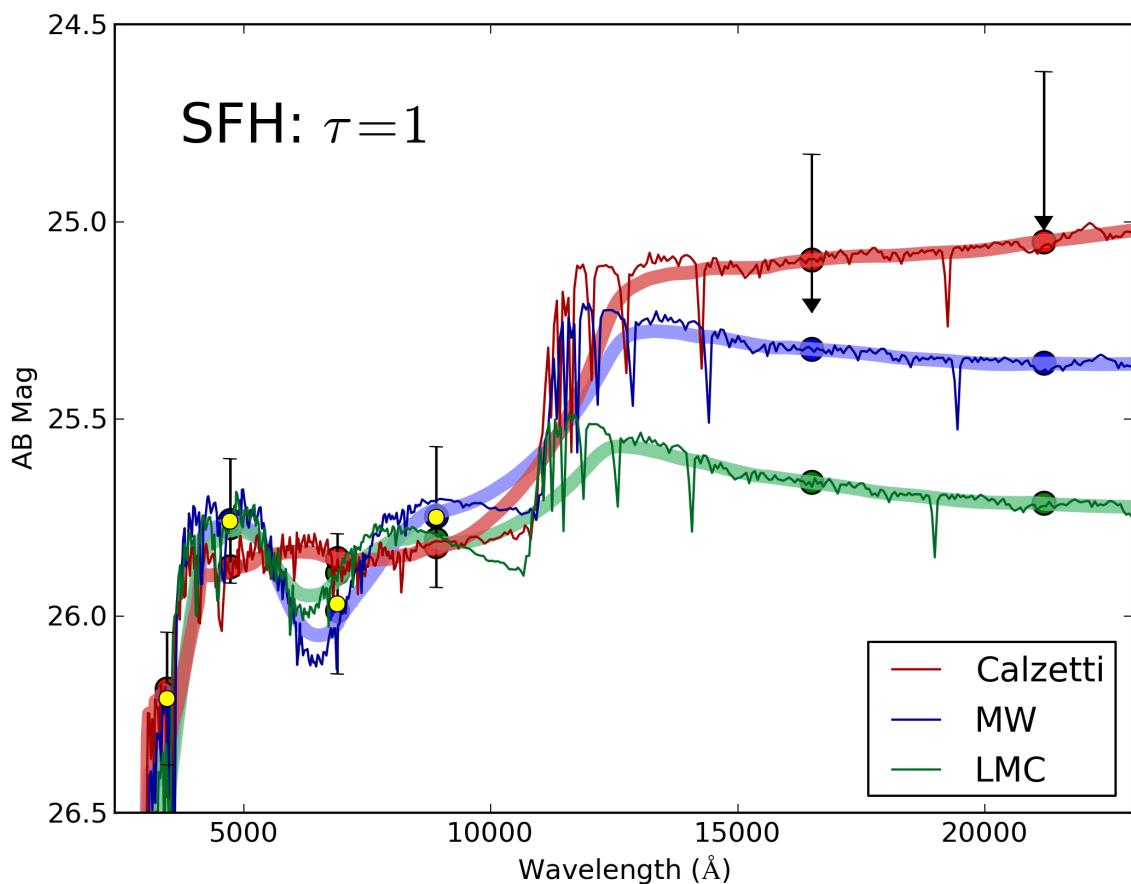
Figure 3.1: Comparison of full resolution spectra and the same spectra convolved with a variable kernel derived from the filter transmission curves of the KDF observations.

to which the spectrum of an object is smoothed by observation through filters, the spectra shown in Figure 3.6 were convolved with a variable kernel which evolved smoothly with wavelength such that at the central wavelengths of each of the $U_n G\mathcal{R}IHK_s$ filters, the kernel was the appropriate FTC and at intermediate wavelengths it was a weighted combination of the surrounding filters (at the shortest and longest wavelengths included, only the closest survey filter was used). The resulting smoothed spectra are shown in Figure 3.1.

3.4   SED fitting of Individual KDF Objects

The three KDF subfields observed by NIRI encompass 36 bBX objects and 161 rBX objects. The IR observations were originally intended to supplement the KDF photometry to sample more of each object's spectrum so that SEDfit could be used to estimate its mass and age. The ranges for these parameters found for the two populations could be compared to those predicted by the downsizing-inspired hypothesis that the strong clustering of bBX objects correlates with their location in massive dark matter halos and that their blue G-$\mathcal{R}$ colour results from the presence of the type of dust which is most likely to coexist with old stellar populations. However, the vast majority of BX-selected objects in the KDF catalogue were not detected so the prominence of the Balmer break could not be measured precisely. The stacking analysis described in section 2.4 was performed to simulate a deeper observation of the prototypical bBX object. While not as precise as it might be with better IR photometry, SED fitting of individual bBX objects can nevertheless constrain the type of dust responsible for their blue G-$\mathcal{R}$ colours. SEDfit was used to fit the $G\mathcal{R}I$ photometry of each bBX object to a grid of models constrained to the redshift range $1.6 \leq z \leq 3.0$. The IR data were excluded because of the higher computational expense of fitting upper limits, which, for these objects, were not expected to provide useful constraints on the models. The U_n data were also omitted because of their sensitivity to highly variable IGM attenuation in the redshift range of BX objects.

If the 2175Å bump (present in the LMC and MW dust laws) is indeed prominent in bBX objects as proposed by Savoy et al. (2011), its use as a potential redshift indicator is an intriguing possibility. Conversely, SED fitting to the photometry of rBX objects is an exercise in futility because of the degeneracy presented by the flatness of the $G\mathcal{R}I$ data: no spectral features are captured by the data which could be used to constrain the redshift and, as mentioned in Section 1.1, three data points are inadequate to exploit a spectrum's flatness. As such, only the bBX objects were considered in the comparison of dust models. Each bBX-selected object in the KDF subfields imaged by NIRI was fit with the set of models described in Section 3.3. Figure 3.2 shows the best fit spectrum to each

KDF#	SFH	Dust Law	$E(B-V)$	z	Age $[\log_{10}(yr)]$	Mass $[\log(M/M_\odot)]$	SFR $[M_\odot/yr.]$
499	$\tau = 1$	LMC	0.15	2.46	7.5	8.9	25.1
550	$\tau = 1$	LMC	0.28	2.26	7.3	8.8	32.7
591	$\tau = 1$	MW	0.10	2.55	8.9	9.7	5.7
592	$\tau = 1$	LMC	0.42	1.90	7.2	8.7	35.1
600	$\tau = 1$	LMC	0.12	2.58	7.3	8.5	16.6
717	$\tau = 1$	LMC	0.37	1.92	6.8	8.5	58.1
749	$\tau = 1$	LMC	0.02	2.28	9.5	10.6	2.5
860	$\tau = 1$	LMC	0.40	1.78	6.5	8.6	116.0
1183	$\tau = 1$	LMC	0.25	2.30	8.1	9.2	14.7
1293	$\tau = -1$	LMC	0.05	2.85	6.8	7.8	11.7
1711	$\tau = 1$	LMC	0.14	1.90	8.8	9.2	2.5
1713	$\tau = 1$	LMC	0.03	1.92	9.2	9.3	0.6
1768	$\tau = 3$	MW	0.10	1.75	8.9	10.0	14.4
2016	$\tau = 1$	LMC	0.20	2.46	6.8	8.9	118.3
2027	SSP	LMC	0.35	2.20	7.1	9.2	0.0
2074	$\tau = 3$	MW	0.40	2.45	9.4	10.9	28.5
2120	$\tau = 3$	Calzetti	0.10	1.75	8.7	9.6	8.9
2161	$\tau = 1$	MW	0.55	1.85	8.8	9.8	9.3
2292	$\tau = 1$	LMC	0.15	1.70	8.1	8.1	1.1
2323	$\tau = 0.1$	Calzetti	0.05	2.15	7.9	8.4	2.5
2364	SSP	MW	0.15	2.80	5.5	8.0	0.0
2384	$\tau = 1$	LMC	0.28	2.48	6.5	9.3	670.9
2449	$\tau = 3$	LMC	0.45	2.05	7.2	8.6	31.4
2505	$\tau = 1$	MW	0.15	2.75	6.5	8.0	31.0
2519	SSP	MW	0.05	2.85	5.4	7.4	0.0
2534	$\tau = 1$	LMC	0.30	2.44	6.3	8.8	350.9
2593	$\tau = 1$	LMC	0.04	2.28	9.4	10.1	1.8
2676	$\tau = 1$	MW	0.20	2.75	6.5	8.0	29.6
2730	$\tau = 1$	LMC	0.27	1.70	7.0	7.7	4.5
2929	$\tau = 0.1$	MW	0.10	2.85	6.4	7.8	26.3
2941	$\tau = 1$	LMC	0.22	2.40	6.8	9.3	300.3
3007	$\tau = 1$	LMC	0.40	1.94	7.9	9.5	44.2
3154	$\tau = 1$	LMC	0.36	1.80	6.1	8.1	113.6
3411	$\tau = 1$	LMC	0.33	1.72	6.4	8.5	114.8
3490	$\tau = 1$	LMC	0.14	1.70	7.9	8.3	2.5
3504	$\tau = 3$	MW	0.20	2.60	7.3	8.5	16.9

Table 3.1: Best-fit model parameters found from SED fitting of individual KDF bBX objects.

Figure 3.2: Plots of overall best fit model (blue) and best model with Calzetti dust (red) for KDF bBX objects. In cases where the best fit model had Calzetti dust, the lines coincide.
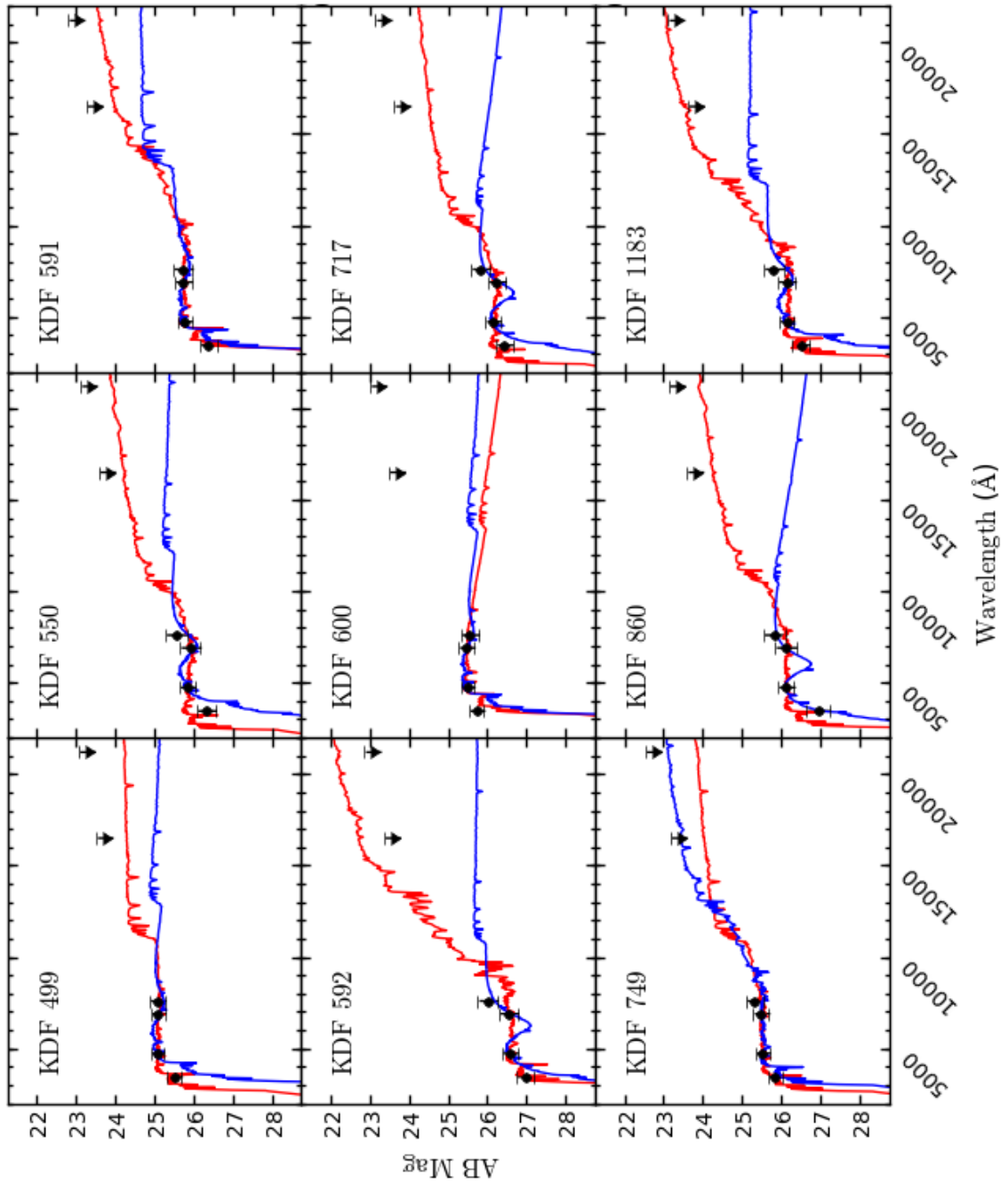
Figure 3.2: Plots of overall best fit model (blue) and best model with Calzetti dust (red) for KDF bBX objects. In cases where the best fit model had Calzetti dust, the lines coincide.

Figure 3.2: Plots of overall best fit model (blue) and best model with Calzetti dust (red) for KDF bBX objects. In cases where the best fit model had Calzetti dust, the lines coincide.
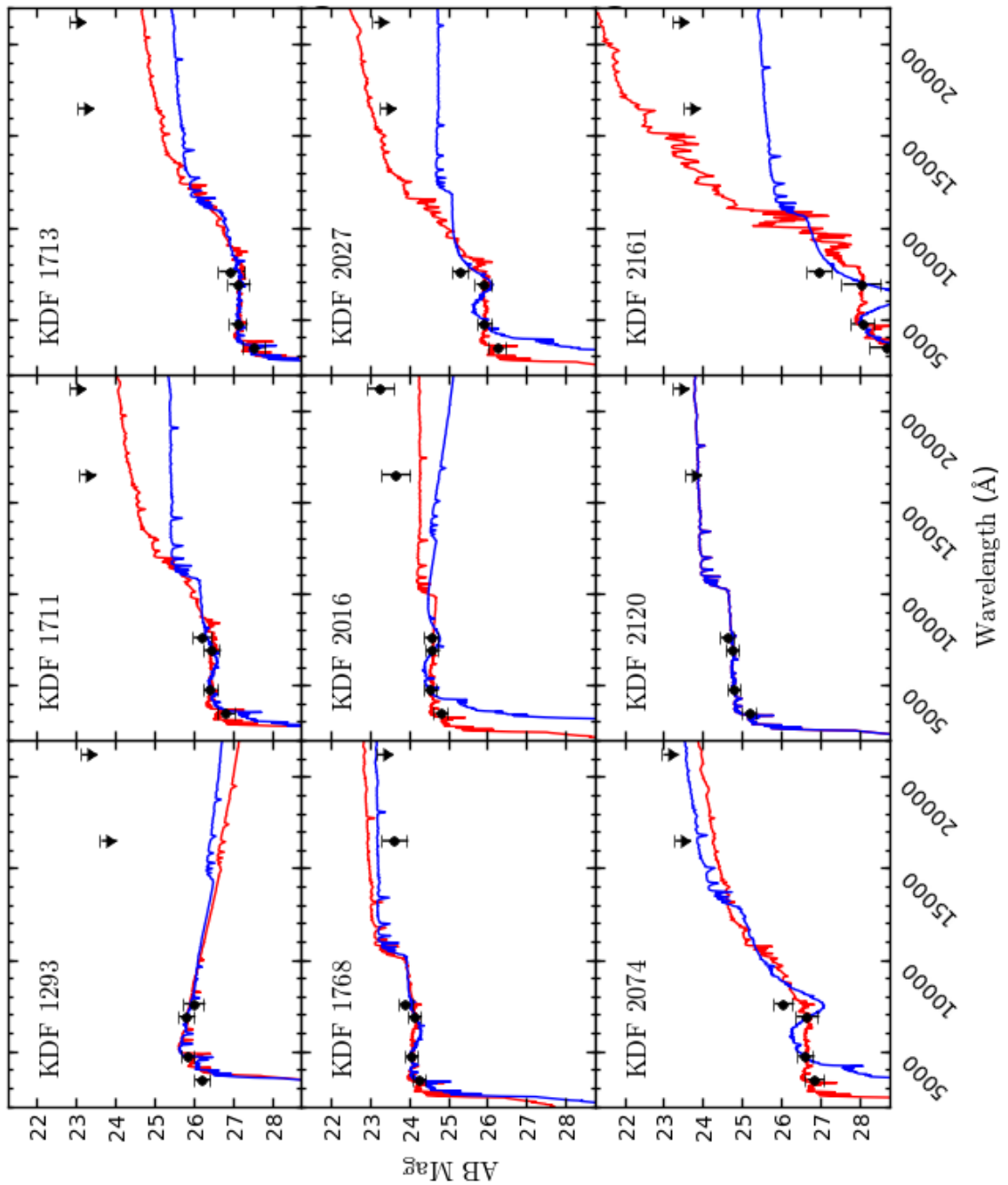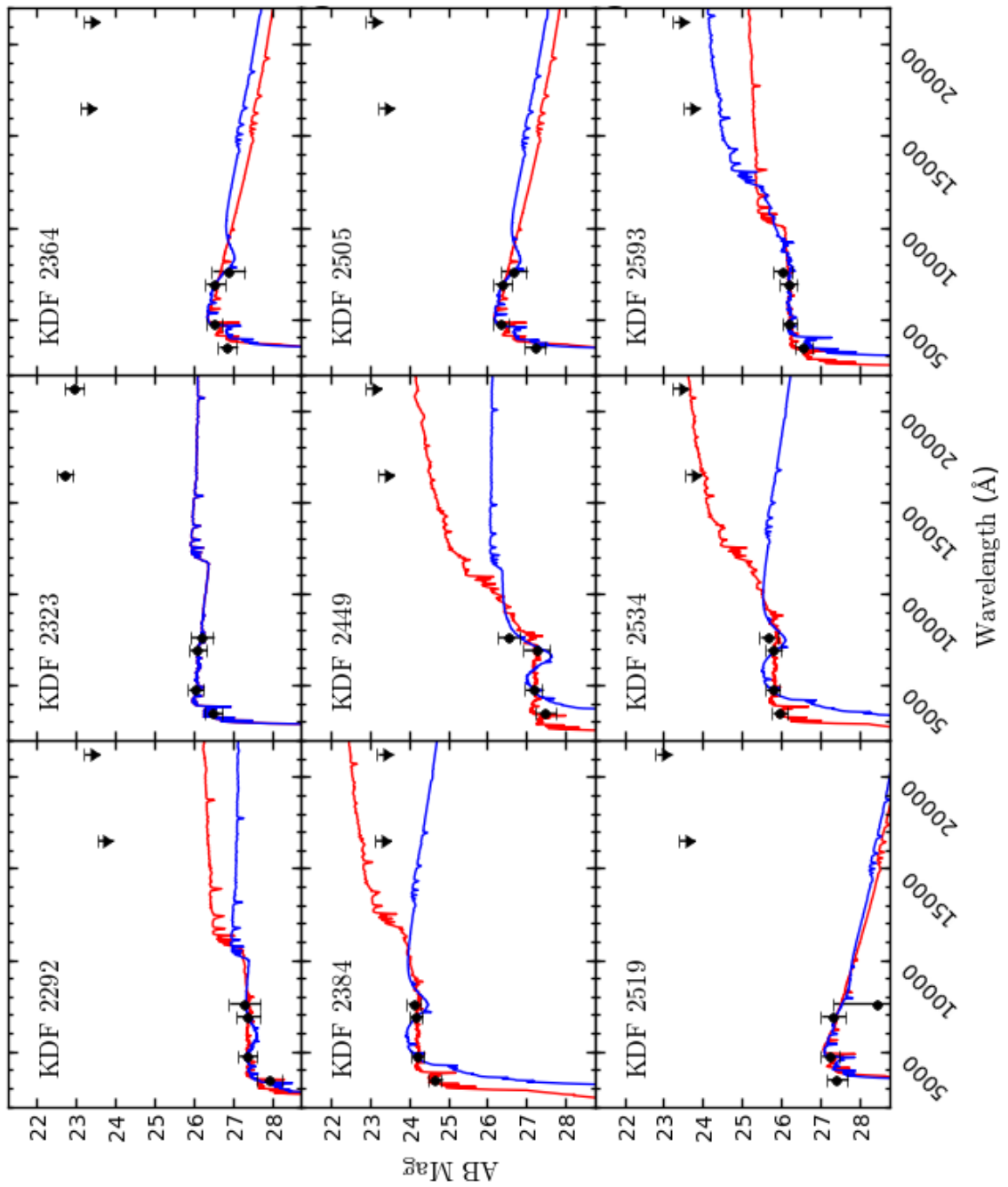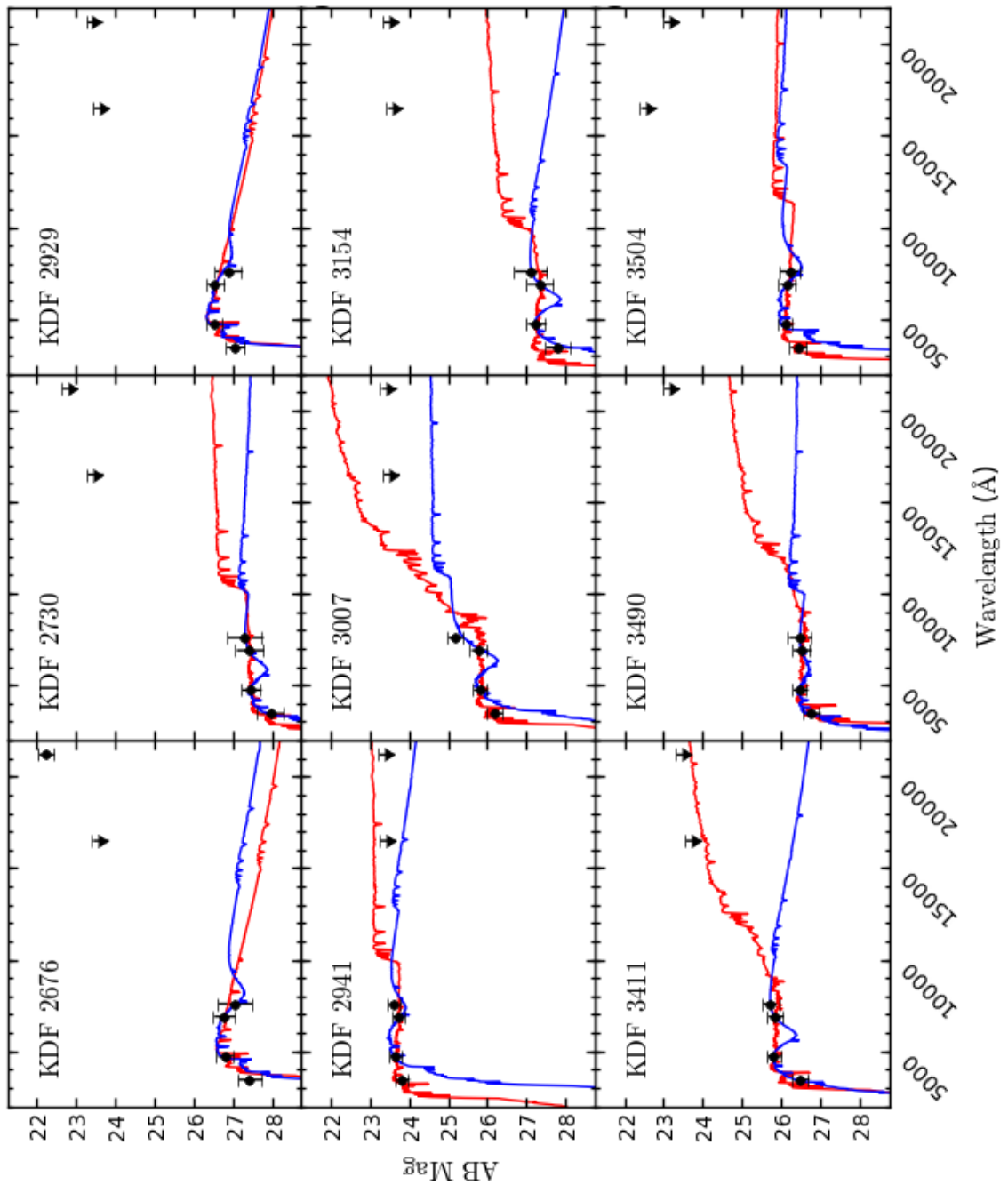
Figure 3.2: Plots of overall best fit model (blue) and best model with Calzetti dust (red) for KDF bBX objects. In cases where the best fit model had Calzetti dust, the lines coincide.

object's photometry and Table 3.1 lists the parameters of these models.

The best fit models have average redshift $\langle z \rangle = 2.2 \pm 0.4$, consistent with the redshift distribution expected for BX-selected samples (Adelberger et al. 2004; Erb et al. 2006; Steidel et al. 2004; Reddy et al. 2005). The distribution of model masses, shown in Figure 3.3, appears to peak below $10^9 \, M_\odot$, somewhat lower than the expected peak value of $\sim 10^{10} \, M_\odot$ found by Shapley et al. (2005) and Steidel et al. (2004) for their samples of BX galaxies. This may indicate that bBX galaxies are inherently less massive than their red counterparts which could place them in less massive DM haloes, contrary to the hypothesis of Savoy et al. (2011). However, the faint limit of each sample must be considered. The BX-selected objects in the KDF subfields considered here have $\langle \mathcal{R} \rangle = 25.7 \pm 1.1$, whereas the BX objects analyzed by Erb et al. (2006) have $\langle \mathcal{R} \rangle = 24.1 \pm 0.7$. The luminosity function calculated for BX objects by Sawicki & Thompson (2006a) indicates that, as is the case locally, faint galaxies are more prevalent than bright galaxies a**t** $z \sim 2$**.** Galaxy mass and luminosity are tightly correlated (Daddi et al. 2007) so it is not surprising that this sample, constructed from much deeper observations, is dominated by low mass objects. Another consideration is the dominance of OB stars in producing the the rest frame UV light seen in the *GRI* region of the spectrum. These stars are young and short-lived so in the absence of data at longer wavelengths where older stellar populations dominate, the ages of these galaxies are highly uncertain and the degeneracy between mass and age becomes important.

Consistent with the hypothesis of Savoy et al. (2011) (that the blueness of bBX galaxies results from the 2175Å bump), the majority of objects in the sample are best fit by models with LMC or MW dust. For some of the best fit models, the amount of dust present is so small that it is not realistically possible to discern which dust law is most appropriate because of the photometric uncertainty. Adopting the criterion $E(B-V) > 0.1$ for significant dust excludes 10 of the KDF bBX objects (591, 749, 1293, 1713, 1768, 2120, 2323, 2519, 2593, 2929). Of the remaining 26 objects, 20 are best fit by models that include LMC dust with $\langle E(B - V) \rangle = 0.28$. The other 6 are best fit by models with MW dust, also with $\langle E(B - V) \rangle = 0.28$. None of the objects with appreciable dust are best modeled with Calzetti dust. These results indicate that the Calzetti model is not the best choice
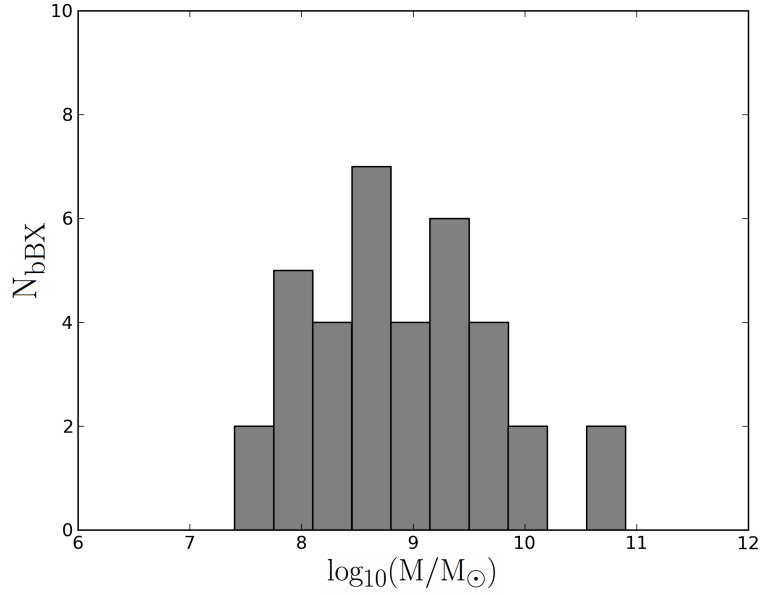
Figure 3.3: Distribution of best fit model masses to KDF bBX objects.

for bBX objects. These objects likely contain significant dust which has an attenuation spectrum including a 2175Å bump that is responsible for their blue G-R colours. This result is independent of star formation history, i.e. the best fitting model with Calzetti dust has a higher χ^2 value than that with MW or LMC dust for all star formation histories in all cases with best fit $E(B-V) \geq 0.1$.

The amount of LMC or MW dust in a galaxy, represented by $E(B-V)$, is reflected in the depth of the 2175Å feature in its spectrum. $E(B-V)$ is therefore expected to correlate with G-R color. Figure 3.4 shows best fit model $E(B-V)$ vs. measured G-R for the bBX objects best fit by MW and LMC dust. The expected correlation is not observed, probably because in most cases the R band does not fall precisely at the maximum of the redshifted 2175Å attenuation bump for a given object. Photometry in a third filter, with central wavelength a few hundred Å longer than that of $\mathcal{R}$, could be used to constrain the depth of the absorption feature by fitting to the known form of the dust model. Better sampling of the bump in this way might also be useful as a redshift indicator for dusty galaxies. This idea is explored in Section 4.2.

The grid of models to which the objects were compared included 6 star formation histories. The
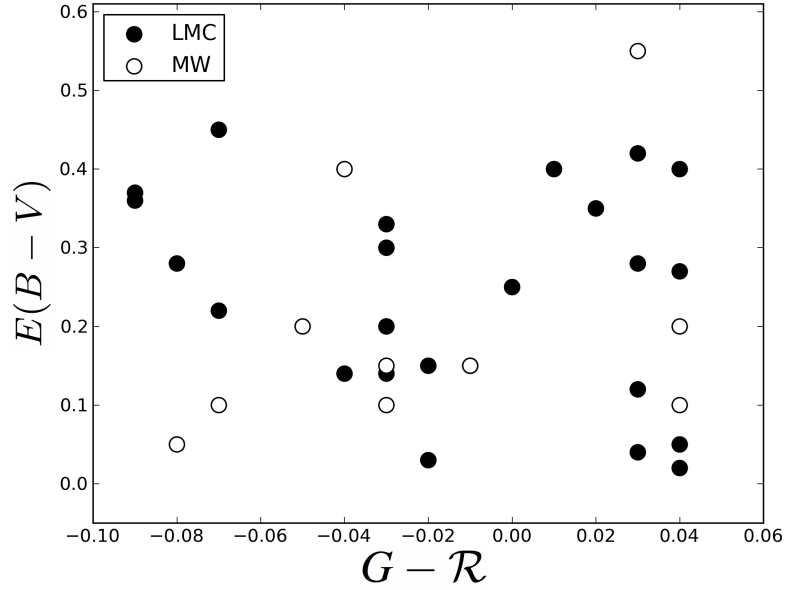
Figure 3.4: $E(B-V)$ of best fit model spectra vs observed $G-\mathcal{R}$ colour of KDF bBX objects for objects best fit with LMC and MW dust models.

MW/LMC dust result is independent of SFH but the sample shows a curious bias toward declining exponential star formation rates in the best fitting models. Whether this is a systematic effect of the SED fitting procedure or a real result is uncertain. As mentioned in Section 1.4, the star formation rate and dust content of a galaxy are not independent: while stars form from cold clouds of dust and gas, fragile dust molecules are destroyed in the presence of strong UV radiation emitted by short-lived O and B stars. The relationship between SFR and dust is extremely complicated, involving the geometry of the system, metallicity, IMF, and specific time-dependent SFH. It is not possible to explain the trend of bBX galaxies being best fit by models with a $\tau = 1$ declining exponential SFH and a dust law with a 2175Å feature in this context. Further, this effect was not observed in the SED fitting analysis of the stacked bBX object or the bBXs with spectroscopically determined redshifts.

3.5 SED fitting of bBX Objects with $H\alpha$ Redshifts

The inherent uncertainty in best fit model parameters derived from SED fitting is significant and it is further increased by the exclusion of the U-band data. Without being able to reliably determine an object's redshift, it is not possible to determine the values of parameters creating the features that define its SED. Ideally, precise redshifts, measured independently, would be used in addition to photometry to constrain model parameters. Whereas no spectroscopic redshifts are available for the KDF bBX objects, the bBX objects in the sample of Erb et al. (2006), introduced in Section 2.5 have redshifts measured from $H\alpha$ line positions. These objects were analyzed similarly to the KDF bBXs to compare the resultant parameters, but with their redshifts fixed at the observed redshift. Consistency between the results should indicate that the redshifts of the KDF objects are not systematically erroneous and affecting the values found for other intrinsic physical properties of the objects.

Each object was fit with the star formation history and dust law found in the analysis of Erb et al. (2006) to ensure comparable results were found for each object. The best fit model parameters found with SEDfit all agreed with those found by Erb et al. (2006) within uncertainty although the two sets of results differ slightly. This may be caused by differences between the model metallicities (Erb et al. (2006) use solar metallicity models whereas this analysis uses $0.4Z_{\odot}$) and between the photometric uncertainties. As mentioned in Section 2.5, uncertainties were not presented with the data so values consistent with those of the KDF observations were adopted. These values do not consider differences in instrumentation, observing conditions or image depths so their assumption could significantly affect the result. The Erb et al. (2006) objects were then fit to the same grid of models (convolved with the appropriate filter transmission curves) as the KDF data. The best fit model parameters found by SEDfit are listed in Table 3.2 with model parameters found by Erb et al. (2006) in brackets. Figure 3.5 shows the photometric data for each object, the best fitting model spectrum (blue) and the best fitting model spectrum with Calzetti dust (red).

Erb et al. (2006) assumed a Calzetti dust law in their SED fitting. The success of LMC and

Identifier	SFH	Dust Law	E(B-V)	$z_{H\alpha}$	Age $[\log_{10}(yr)]$	Mass $[\log(M/M_\odot)]$	SFR $[M_\odot/yr]$
HDF-BX1376	$\tau = 1$	Calzetti	0.12	2.42	8.1 (8.4)	9.5 (9.3)	31.2 (9)
HDF-BMZ1156	$\tau = 1$	N/A	0.00	2.22	9.5 (9.3)	11.0 (11.0)	5.3 (4.)
Q1623-BX432	Constant SF	Calzetti	0.14	2.18	8.7 (9.1)	10.0 (9.9)	23.6 (6)
Q2343-BM133	Constant SF	LMC	0.26	1.48	7.4 (8.2)	9.7 (9.7)	217.1 (35)
Q2343-BX163	SSP	MW	0.28	2.12	6.0 (9.2)	9.9 (10.1)	0.0 (9)
Q2343-BX418	Constant SF	N/A	0.00	2.3	8.7 (7.9)	9.7 (9.0)	11.0 (12)
Q2343-BX599	SSP	MW	0.41	2.02	6.0 (9.2)	10.4 (10.5)	0.0 (21)
Q2343-BX660	$\tau = 1$	MW	0.06	2.18	9.2 (9.4)	10.4 (10.1)	11.0 (5)
Q2343-MD80	SSP	MW	0.70	2.02	5.9 (8.4)	10.2 (9.8)	0.0 (1)

Table 3.2: Best fit model parameters from SEDfitting to Erb et al. (2006) bBX objects at fixed redshift. Bracketed values beside the best fit values for Age, Mass, and SFR are those found by Erb et al. (2006) assuming constant star formation and Calzetti et al. (2000) dust.

MW dust in fitting the KDF bBX objects suggested that many of the objects they analyzed would be better fit by models that included the 2175Å dust feature. After discounting those objects whose best fit models have negligible dust ($E(B - V) \leq 0.1$), 6 objects remain. Of these, 2 are best fit with Calzetti dust (but with values of $E(B - V) = 0.12$ and 0.14), 3 with MW dust, and one with LMC dust. While the sample is very small, this result indicates that many dusty high-redshift galaxies are misrepresented by models that do not include the 2175Å bump.

Three of the 9 objects are best fit by models with declining exponential star formation histories, suggesting that the overwhelming number of KDF bBX objects best fit by $\tau = 1$ models is anomalous and possibly indicative of a systematic error.

3.6 SED fitting to stacked object photometry

The photometry of the average stacked bBX object, described in section 2.4, was fit to the same grid of models as the individual KDF objects (minus those with declining exponential star formation rates with $\tau = 0.1$). In these fits, the U-band photometry (excluded in the case of individual objects) was considered as were the IR upper limits. Because many lines of sight were averaged to create the image the assumption of average intergalactic attenuation is appropriate. The average stacked bBX

Figure 3.5: Plots of overall best fit model (blue) and best model with constant star formation and Calzetti dust (red) for Erb et al. (2006)bBX objects. In cases where constant SF and Calzetti dust gave the best fit, the lines coincide.
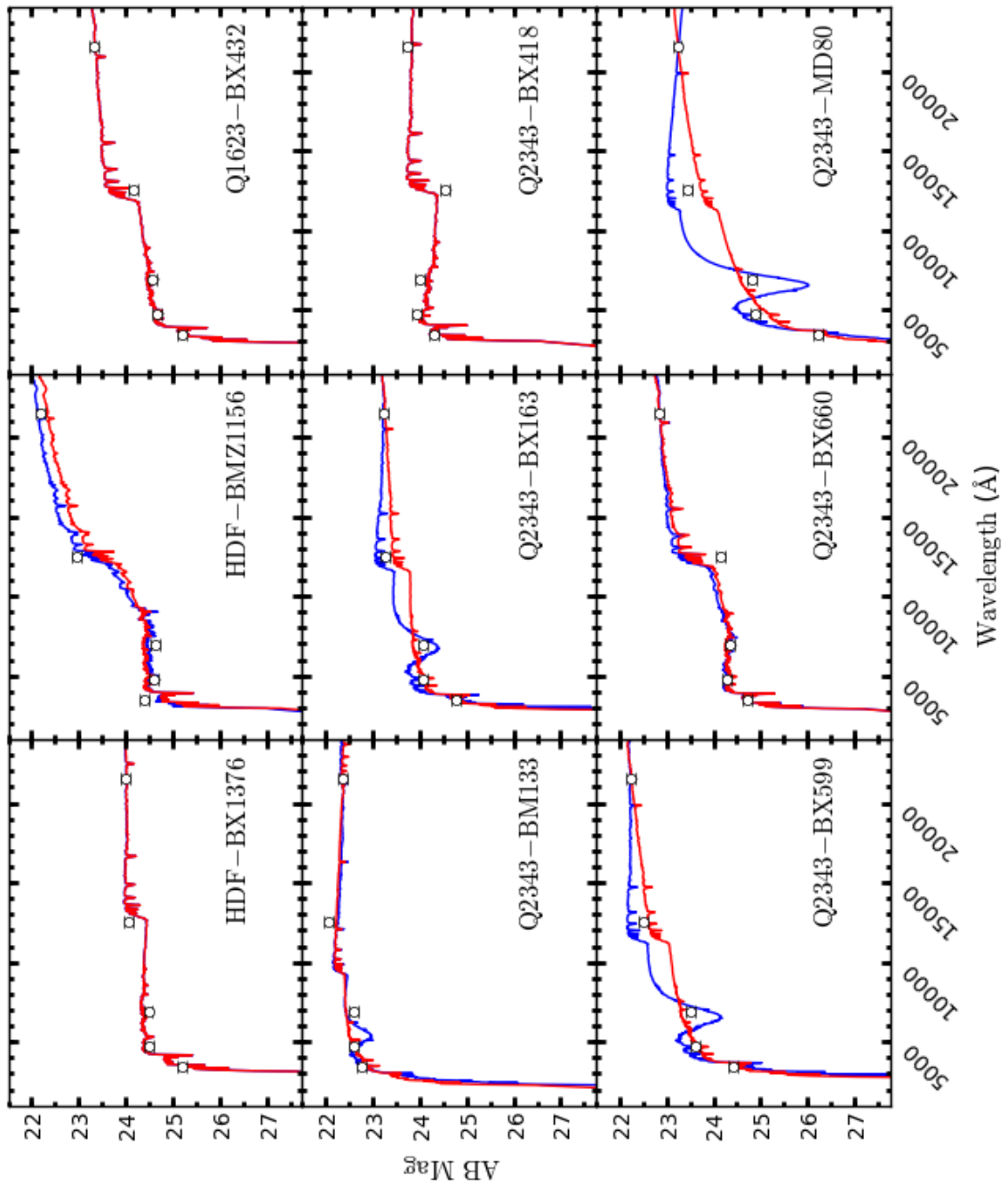
image is still undetected at 1σ in H and K but the faint limits provide tighter constraints because of the $\sqrt{n_{\text{objects}}}$ improvement in the signal to noise ratio (SNR). These fainter detection limits are useful in ruling out portions of the model parameter space so the fits were run using SEDfit's option for treating upper limits with a downhill gradient search algorithm. The parameters of the best fitting model for each combination of star formation history and dust law are summarized in Table 3.3 and the corresponding SEDs are plotted in Figure 3.6 with the bBX average stack photometry.

For all SFH/dust combinations, the best fit redshift of models to the bBX average stack (listed in Table 3.3) agrees with the mean best fit redshift of the fits to the individual KDF bBX objects ($\langle z \rangle = 2.06 \pm 0.47$), and that of the Erb et al. (2006) sample of Hα redshifts for bBX galaxies ($\langle z \rangle = 2.18 \pm 0.14$). However, the best fit redshifts are all ≤ 2.0, on the lower side of the expected range. To investigate the possibility that this indicates that the global minimum of χ^2 in the parameter space was not being found by the optimization algorithm, SEDfit was run on the photometry again with redshifts forced to be within one standard deviation of the mean spectroscopic redshift of the 9 bBX objects from Erb et al. (2006). In this case, all best-fit models were located at the minimum permitted redshift and had χ^2 values marginally higher than they did when the redshift constraint was not in place. This may indicate that bBX objects are located at lower redshift than rBXs, or, more likely, that the average IGM attenuation of the 36 lines of sight of the objects is not equal to the value prescribed by Madau (1995). It is also possible that neither the MW or LMC dust law accurately describes attenuation in these galaxies and a different parametrization of the continuum and 2175Å feature is required, such as that used by Buat et al. (2012a).

The overall best-fit model to the average stack photometry is a single burst of star formation with age 1 Myr at $z = 2.0$. Section 4.1 considers the redshift ranges over which model galaxies would be selected with the bBX criteria. The best fitting model would, theoretically, never be selected as a bBX object. It is also extremely young, having an age of only $10^{6.2}$ years, which represents a minuscule fraction of the lifetime of a galaxy. Observing galaxies so soon after formation is very rare. It is, therefore, highly improbable that all of the bBX galaxies are so young. The SSP/MW model is therefore unlikely to describe the typical bBX

SFH	Dust Law	z	$E(B-V)$	Age $[\log_{10}(\mathrm{yr})]$	Mass $[\log_{10}(\mathrm{M/M_\odot})]$	SFR $\mathrm{M_\odot/yr}$	$\chi^2 - \chi^2_{\min}$
	Calzetti	1.78	0.00	6.2	8.8	0.0	0.84
SSP	MW	2.00	0.15	6.0	8.5	0.0	0.00
	LMC	1.86	0.16	5.9	8.1	0.0	0.38
	Calzetti	1.93	0.08	8.7	9.2	3.3	1.36
Const.	MW	1.97	0.15	8.2	8.9	5.9	0.04
	LMC	1.89	0.13	8.0	8.7	5.1	0.37
	Calzetti	1.93	0.08	8.7	9.2	3.1	1.32
$\tau = 1$	MW	1.96	0.15	8.3	9.0	5.6	0.04
	LMC	1.89	0.14	7.9	8.6	5.9	0.37
	Calzetti	1.93	0.08	8.7	9.1	3.3	1.35
$\tau = 3$	MW	1.99	0.14	8.3	8.9	5.5	0.04
	LMC	1.90	0.12	8.1	8.7	4.7	0.37
	Calzetti	2.00	0.08	8.5	8.8	3.0	1.41
$\tau = -1$	MW	1.97	0.15	8.1	8.7	5.4	0.04
	LMC	1.84	0.20	6.9	8.1	15.1	0.36

Table 3.3: Best fit model parameters from SED fitting to average bBX object stack photometry.

object. Four other models have values of χ^2 just 0.04 higher than the best fitting model: MW dust with constant star formation, exponentially declining star formation with $\tau = 3$ or $\tau = 1$, and exponentially increasing star formation with $\tau = 1$. These four models have consistent ages ($\log_{10}(\mathrm{age/year}) = 8.2, 8.3, 8.3, 8.1$), masses ($\log_{10}(\mathrm{M/M_\odot}) = 8.9, 9.0, 8.9, 8.7$), and dust attenuations ($E(B-V) = 0.15, 0.15, 0.14, 0.15$). This consistency suggests that these parameters are likely more representative of the typical bBX galaxy than those of the best fitting model but that it is not possible to infer star formation history from these data. There is likely a fairly flat extended parameter space which hosts nearly equally acceptable models. However, while many models have $\chi^2 \sim \chi^2_{min}$, none of these includes Calzetti et al. (2000) dust.

3.7 Summary of Analysis

This chapter presents the results of SED fitting of the photometric data of bBX objects from 3 samples: objects in the KDF IR subfields, the average object obtained by stacking the images of the KDF bBXs, and bBX objects from the data of Erb et al. (2006). Each of these analyses
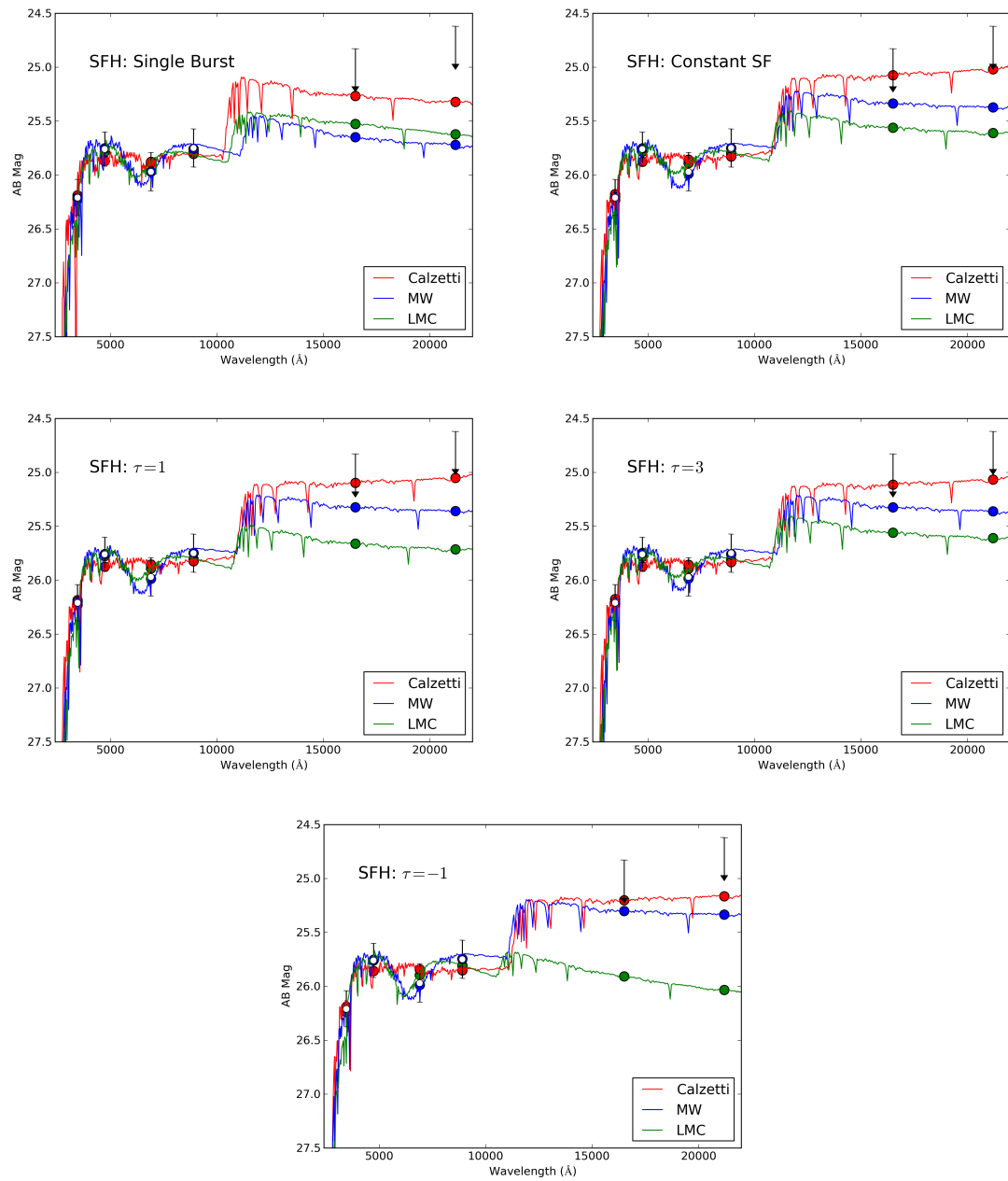
Figure 3.6: Best fit spectra from SEDfitting to average bBX object stack photometry for 5 star formation histories.

suggests that many of the bBX objects contain dust that is not well-represented by the Calzetti et al. (2000) attenuation law that has generally been assumed for star forming galaxies at high redshift (e.g. (Jaacks et al. 2012; Michalowski et al. 2012; Wake et al. 2011; Zhao et al. 2011; Finlator et al. 2010; Sawicki & Thompson 2006b; Shapley et al. 2005)). This result supports the hypothesis presented in Savoy et al. (2011) that bBX galaxies have a prominent 2175Å bump. The next Chapter will examine its significance to past and future observations.

Chapter 4

Implications of a 2175Å Dust Feature in bBX Galaxies

The analysis described in Chapter 3 suggests that many of the bBX galaxies contain 2175Å dust features. In this chapter, some consequences of this that impact past and future analyses are considered.

4.1 The Impact of Dust on Clustering Measurements

The study of star-forming galaxies at high redshifts has generally assumed that these objects contain Calzetti dust (e.g. Jaacks et al. 2012; Michalowski et al. 2012; Wake et al. 2011; Zhao et al. 2011; Finlator et al. 2010; Sawicki & Thompson 2006b; Shapley et al. 2005). However, even from the meager photometry considered, it is abundantly clear that many of the bBX objects analyzed here are better modeled by a dust law that includes the 2175Å absorption feature. Because many properties of galaxies at high redshift have been inferred assuming the absence of the bump, it is important to revisit these conclusions. Here, the effect of changing the dust law on clustering measurements is examined.

The redshift range of an observed population is derived from physical properties assumed for

the sample, including the effect of dust on its SED. It is thus necessary to revise the redshift range assumed for bBX galaxies to determine whether the curiously strong clustering of bBX objects found by Savoy et al. (2011) is affected. To consider this question, GALAXEV population synthesis models for three star formation histories (constant star formation, a single stellar population, and declining exponential star formation with $\tau = 1$) were generated for a range of ages encompassing those found for the bBX objects. SEDfit was used to apply average Madau (1995) IGM attenuation and Calzetti, LMC, and MW dust attenuation for values of $E(B - V)$ from 0 to 0.5. The SEDs were then redshifted from z=0 to z=5 and convolved with the Keck filter transmission curves to simulate the KDF photometry. The photometry of each model at each redshift was compared to the BX selection criteria to determine the range of redshifts over which each rest-frame model could fall into the selection window.

Figure 4.1 shows the progression of the models in (*U-G*) (*G-R*) space from $z = 0$ to $z = 3$ for various ages. The colour of points corresponds to model redshift, ranging from blue at $z = 0$ to red at $z = 3$. The size of points in each track corresponds to the value of $E(B - V)$ of a model. In each panel, four tracks are plotted corresponding to $E(B - V) = 0.00, 0.15, 0.30, 0.45$ in the dust law indicated. The light shaded region corresponds to the rBX selection window and the darker region to the bBX window. Figure 4.2 shows the redshift ranges of rBX and bBX for the same models but serves to emphasize the changing redshift range of BX models with changing dust laws. Here, the red and blue bars represent the redshift ranges of rBX and bBX selected models, respectively.

The complications introduced by the inclusion of the 2175Å feature in a model are clearly illustrated in Figure 4.1. A value of $E(B - V) = 0$ represents the absence of dust so for a given model, the first model track for each dust law is identical. The combination of Calzetti dust and constant star formation has conventionally been used to represent star forming systems at high redshift. Increasing the amount of dust in this model results in a tidy translation of the corresponding track in $(U - G)$ $(G - \mathcal{R})$ space such that the range of redshifts spanned by BX-selected models is roughly constant. For models including a 2175Å dust feature, this is no longer the case: increasing dust produces an overlapping set of model tracks which pass through the BX-selection region

Figure 4.1: Redshift evolution of model galaxies in $(U - G)/(G - R)$ space for various dust laws and values of E(B-V). The colour of each point represents redshift from blue at $z = 0$ to to red at $z \sim 3$. The four point sizes correspond to values of $E(B - V) = 0.0, 0.15, 0.30 \, \text{and} \, 0.45$. The grey shaded region corresponds to the BX selection colour criteria defined in Equation 1.1, with the darker region representing the additional bBX criterion.

Figure 4.1: Redshift evolution of model galaxies in $(U - G)/(G - \mathcal{R})$ space for various dust laws and values of E(B-V). The colour of each point represents redshift from blue at $z = 0$ to to red at $z = 3$. The four point sizes correspond to values of $E(B - V) = 0.0, 0.15, 0.30$ and 0.45. The grey shaded region corresponds to the BX selection colour criteria defined in Equation1.1, with the darker region representing the additional bBX criterion.

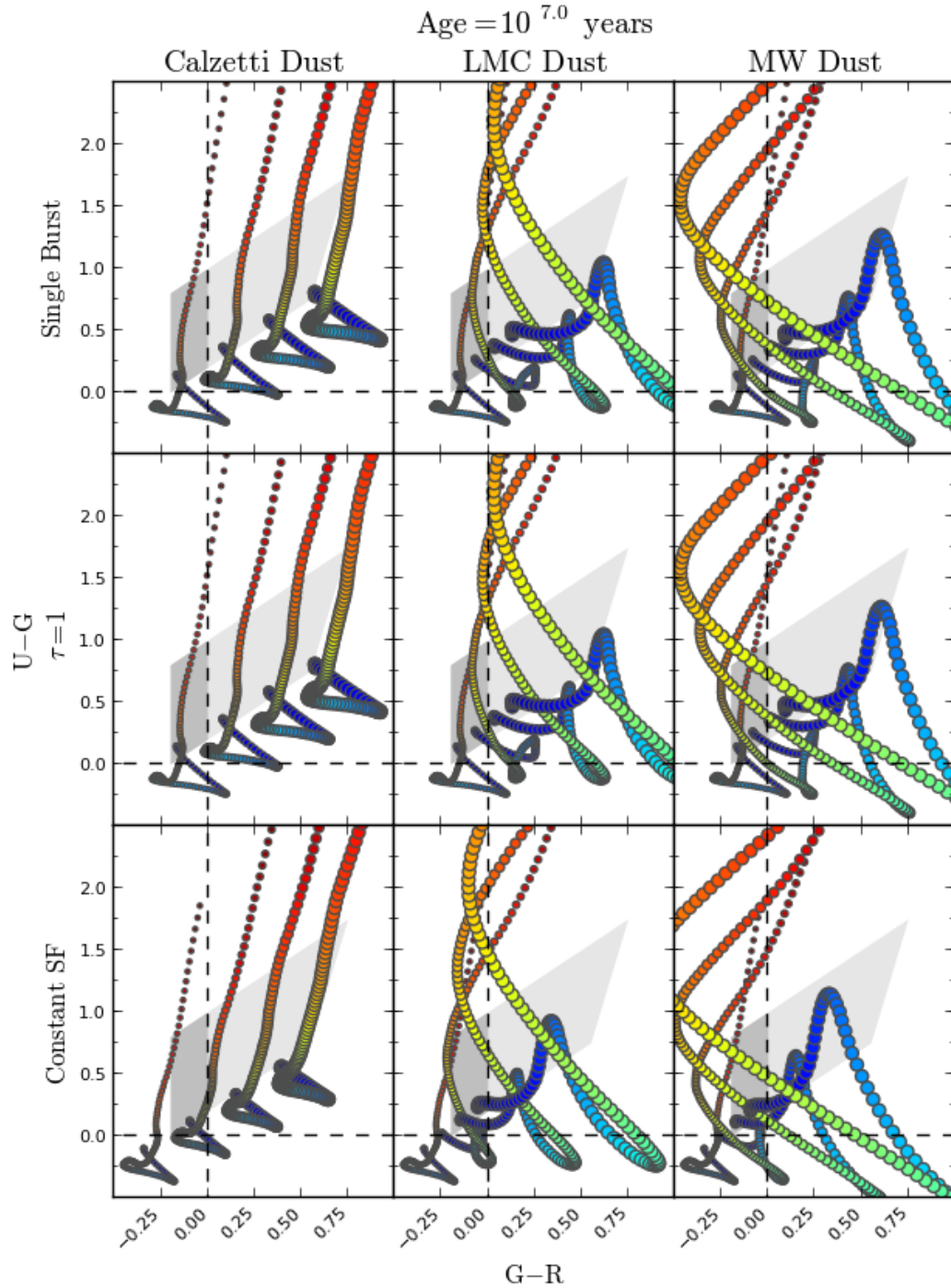Figure 4.1: Redshift evolution of model galaxies in $(U - G)/(G - \mathcal{R})$ space for various dust laws and values of E(B-V). The colour of each point represents redshift from blue at $z = 0$ to to red at $z = 3$. The four point sizes correspond to values of $E(B - V) = 0.0, 0.15, 0.30$ and 0.45. The grey shaded region corresponds to the BX selection colour criteria defined in Equation1.1, with the darker region representing the additional bBX criterion.
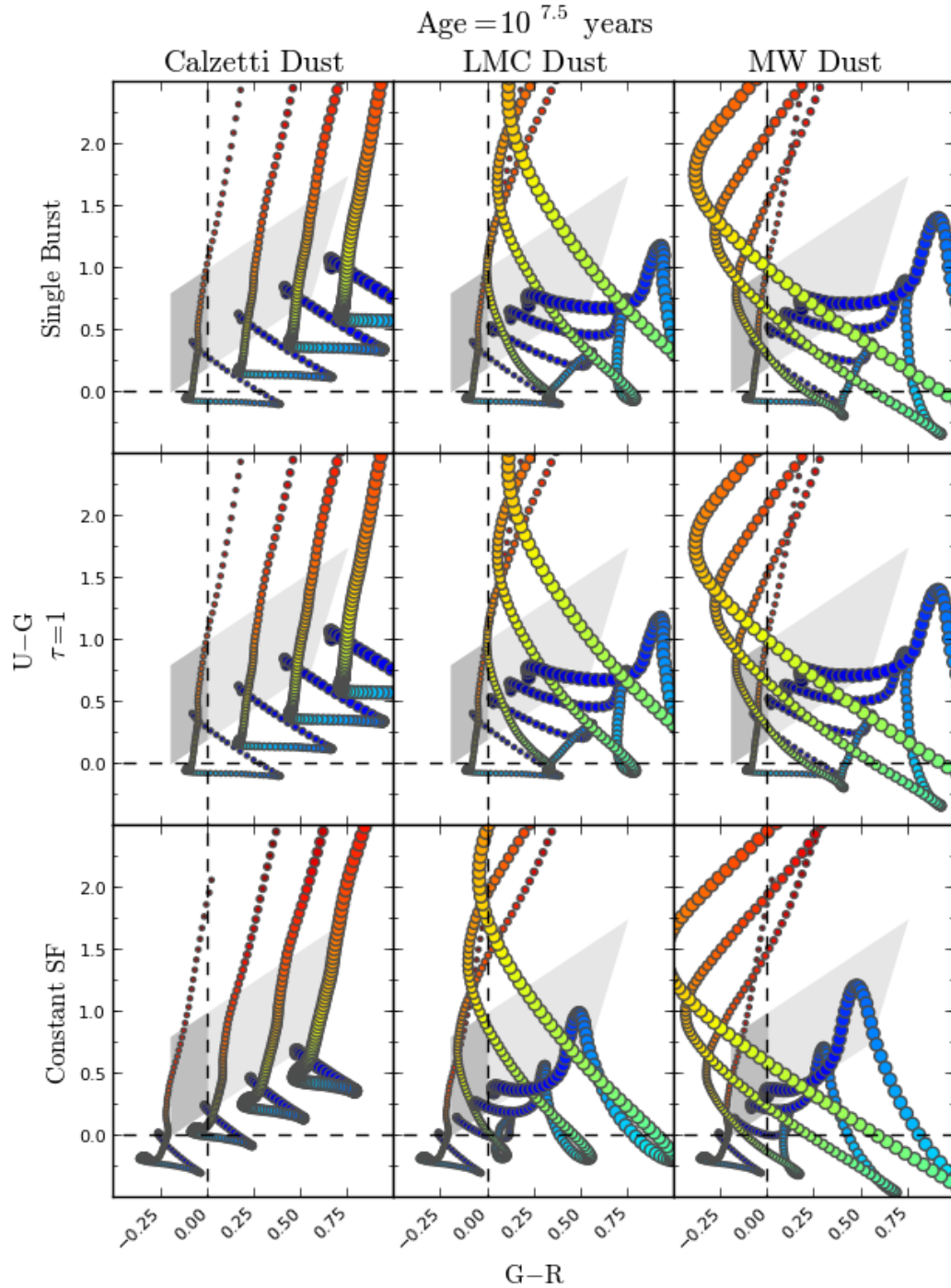
Figure 4.1: Redshift evolution of model galaxies in $(U-G)/(G-\mathcal{R})$ space for various dust laws and values of E(B-V). The colour of each point represents redshift from blue at $z = 0$ to to red at $z = 3$. The four point sizes correspond to values of $E(B-V) = 0.0, 0.15, 0.30$ and 0.45. The grey shaded region corresponds to the BX selection colour criteria defined in Equation1.1, with the darker region representing the additional bBX criterion.
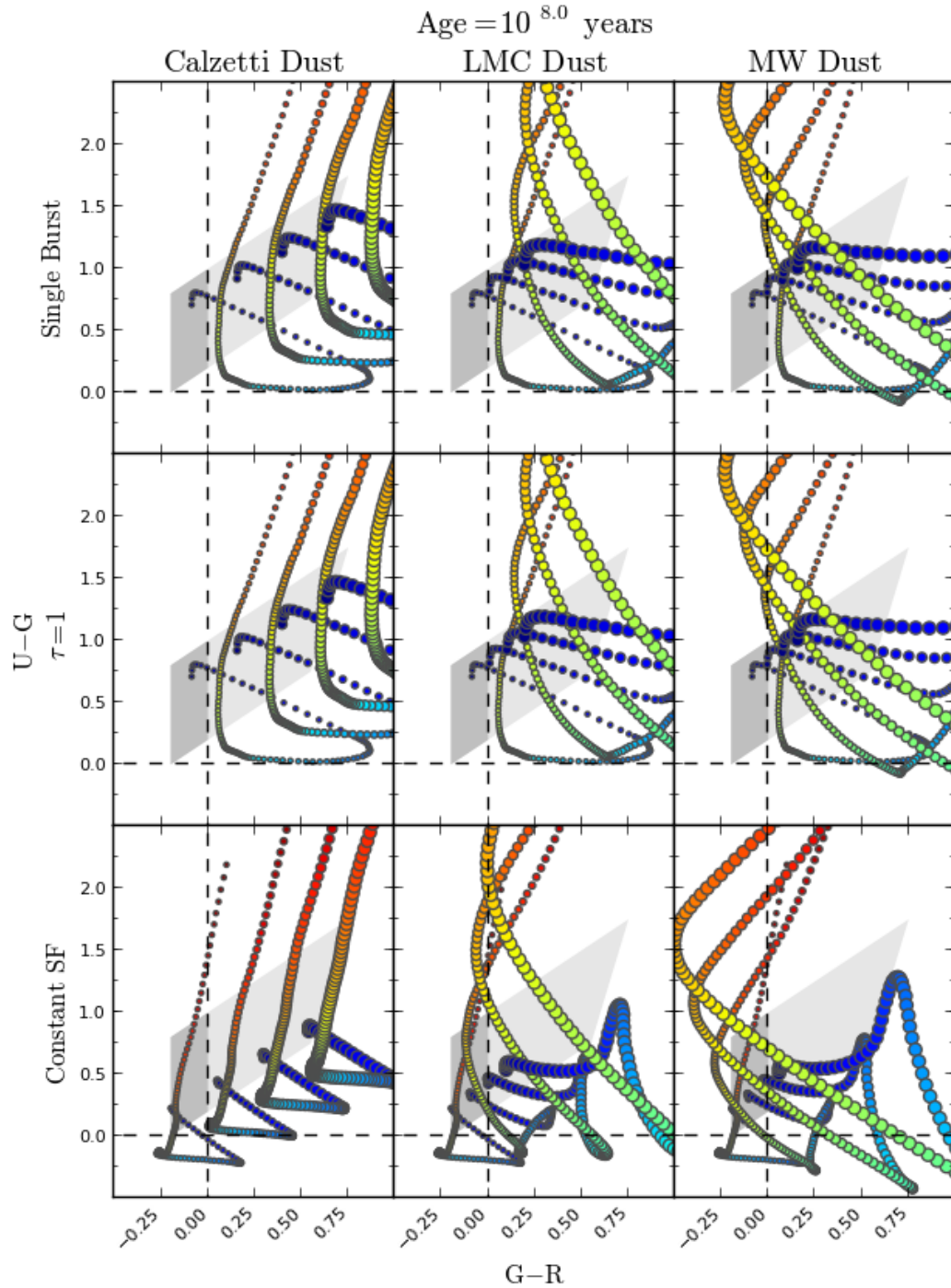
Figure 4.2: Redshift ranges over which model galaxies with various parameters will be meet the bBX or rBX selection criteria. The bBX and rBX criteria are mutually exclusive: red and blue bars represent rBX and bBX objects respectively. Black bars represent their union.

Figure 4.2: Redshift ranges over which model galaxies with various parameters will be meet the bBX or rBX selection criteria. The bBX and rBX criteria are mutually exclusive: red and blue bars represent rBX and bBX objects respectively. Black bars represent their union.

Figure 4.2: Redshift ranges over which model galaxies with various parameters will be meet the bBX or rBX selection criteria. The bBX and rBX criteria are mutually exclusive: red and blue bars represent rBX and bBX objects respectively. Black bars represent their union.
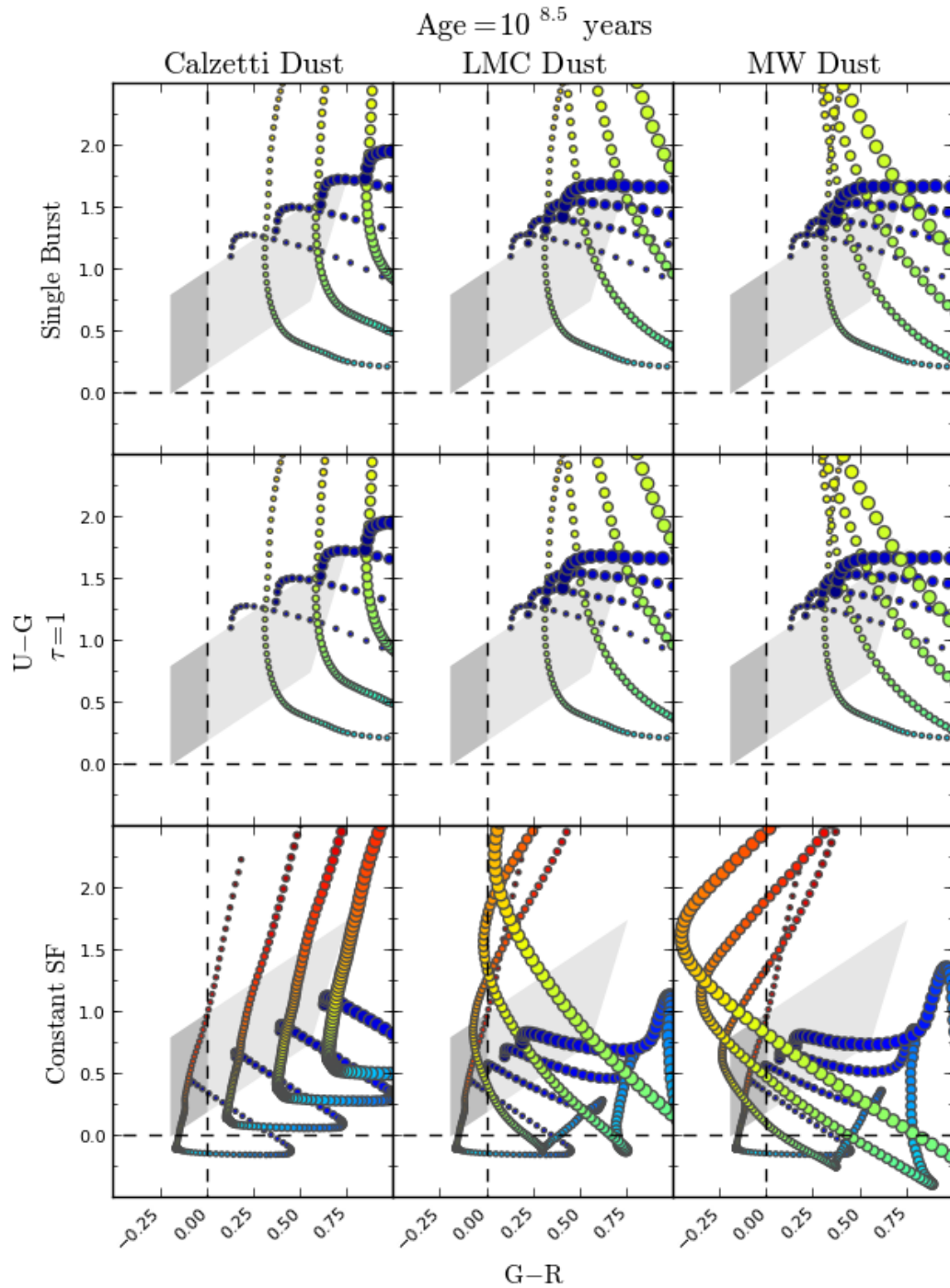
Figure 4.2: Redshift ranges over which model galaxies with various parameters will be meet the bBX or rBX selection criteria. The bBX and rBX criteria are mutually exclusive: red and blue bars represent rBX and bBX objects respectively. Black bars represent their union.
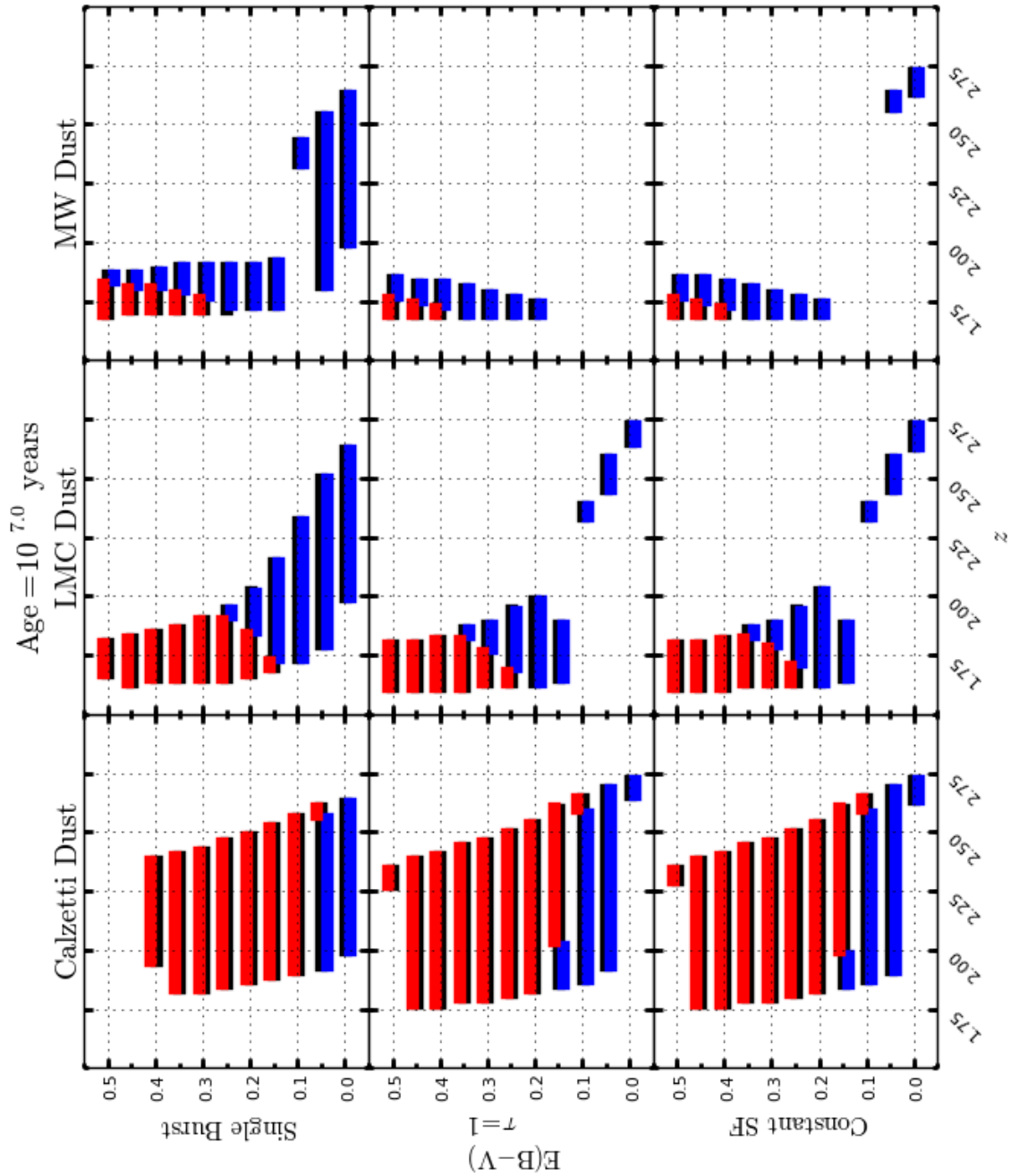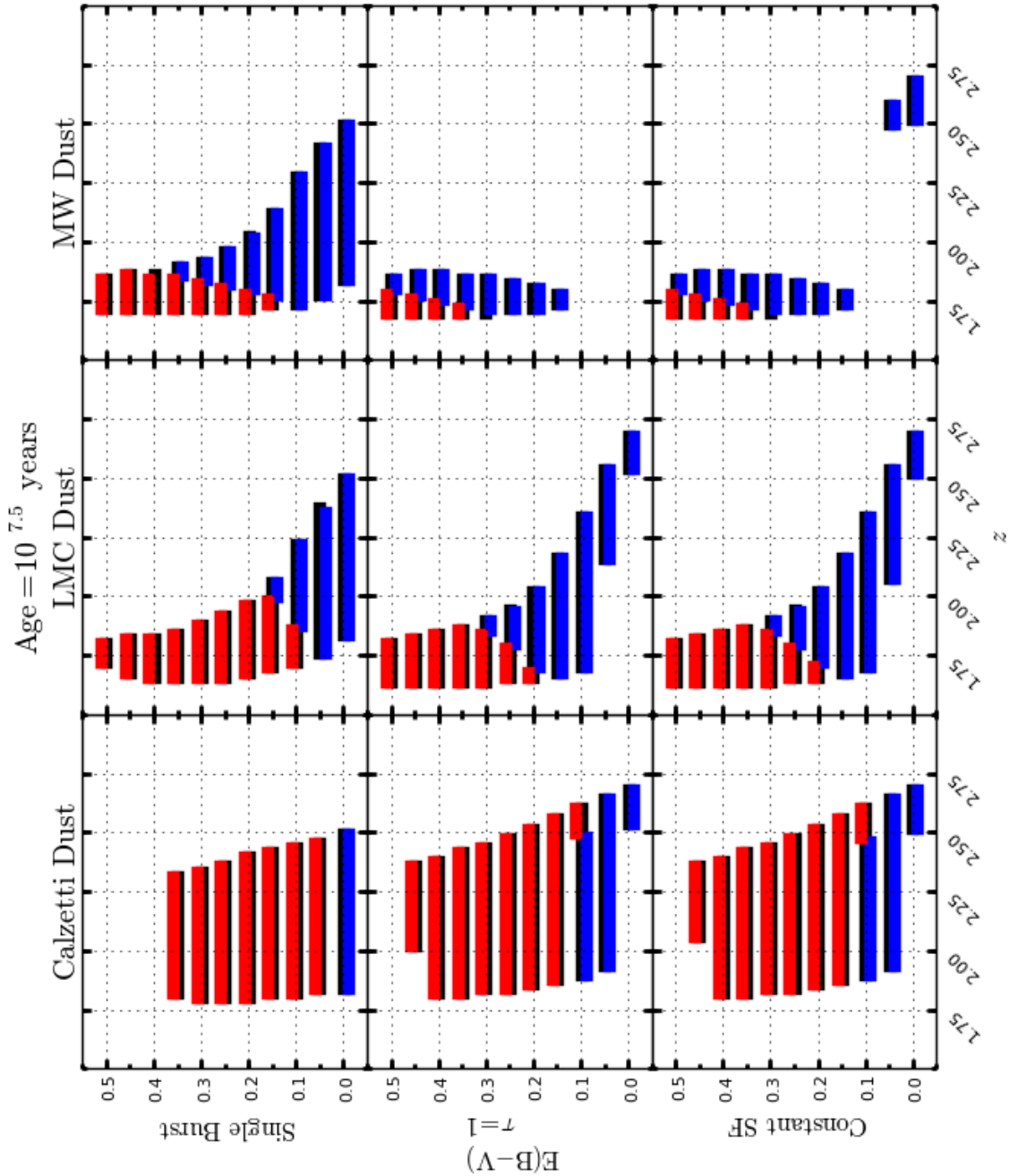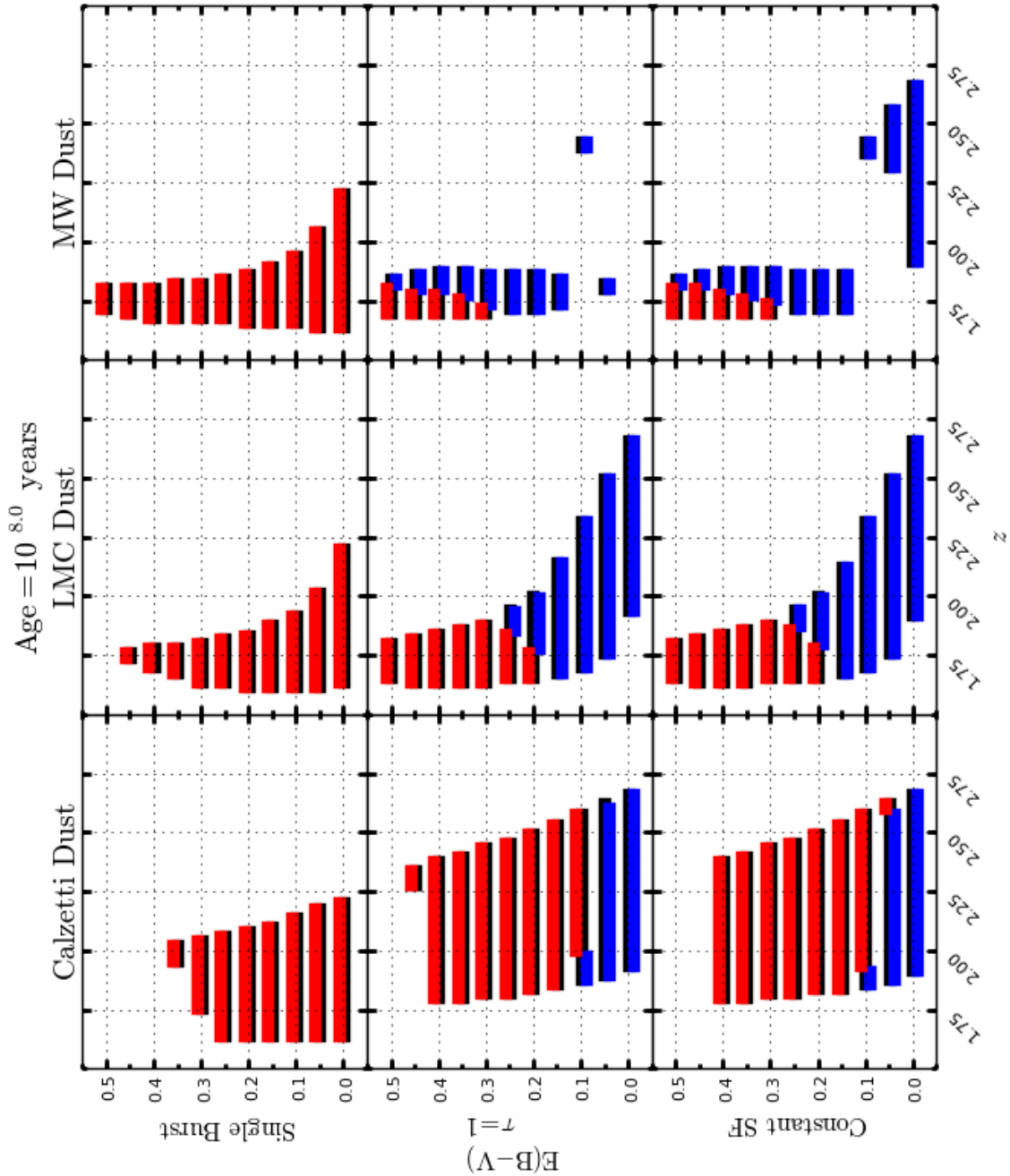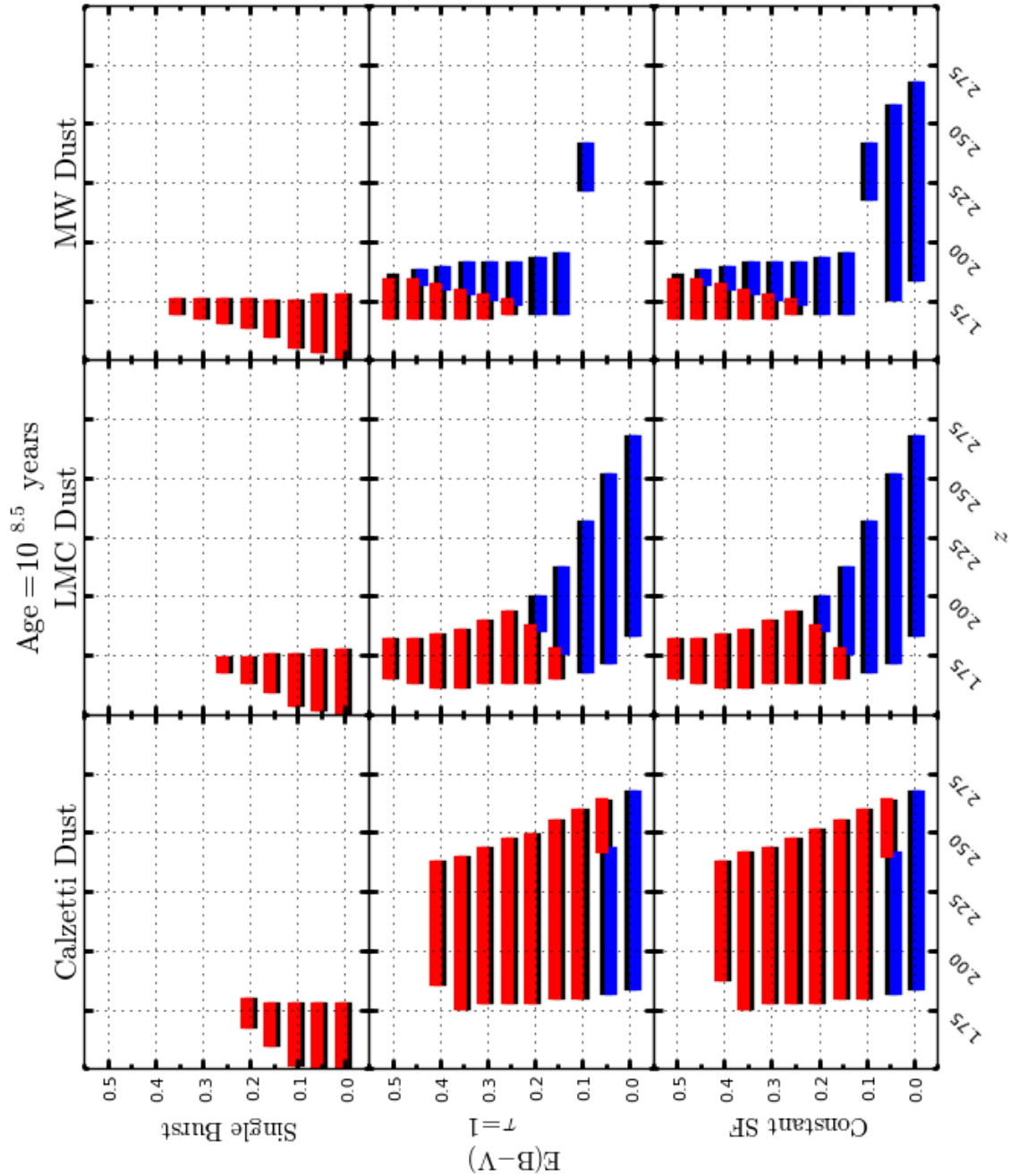
over highly variable redshift ranges. These ranges determine the limits of integration used to deproject a measurement of angular clustering strength to determine a spatial correlation length so this variability could have a significant impact on the results of clustering analyses. In some cases the model track passes through the selection window at very low redshift. In the analysis that follows, only the redshift range near $z \sim 2$ is considered.

While a complete reanalysis of colour-dependent clustering is beyond the scope of this work, it is possible to demonstrate that changing the redshift range of the bBX population can have an effect on clustering measurements by considering the limits of integration used in the analysis of Savoy et al. (2011). Note that the goal of these calculations is merely to show that an effect exists, not to determine its magnitude precisely. To do so would require a full clustering reanalysis of multiple populations and is beyond the scope of this project.

To calculate the spatial clustering strength of a sample, it is first necessary to measure its *angular* two-point correlation function, A_ω, which measures the number of unique pairs of galaxies separated by a given angular distance compared to those in a random distribution. To compute A_ω the distribution of objects belonging to a population in an image is compared to a randomly generated distribution with the same geometry. Additional, unclustered objects are randomly added to the image and then A_ω is determined by examining the number of pairs of galaxies with a given separation. Savoy et al. (2011) use the estimator of Landy & Szalay (1993), conventionally used to measure galaxy clustering at high redshift:

$$w_{\mathrm{LS}}(\theta) = \frac{DD(\theta) - 2DR(\theta) + RR(\theta)}{RR(\theta)}, \tag{4.1}$$

where $DD(\theta)$, $DR(\theta)$, and $RR(\theta)$ are the number of data-data, data-random, and random-random galaxy pairs with angular separations between $\theta - \Delta\theta$ and $\theta + \Delta\theta$. On large scales, a power law of the form

$$w(\omega) = A_\omega \theta^{-\beta} \tag{4.2}$$

can be used to approximate the correlation function. The desired parameter is the physically meaningful counterpart of this angular quantity: the spatial correlation function, $r_0(z)$, which accounts for the 3-dimensional distribution of the objects within a specific cosmological model. It is related to the angular correlation function through the Limber inversion (Totsuji & Kihara 1969) :

$$A_\omega = \frac{H_\gamma r_0^{1-\gamma} \int F(z) r_c^{1-\gamma}(z) N^2(z) E(z) dz}{\frac{c}{H_0} \left[\int N(z) dz \right]^2},$$

(4.3)

where $r_c(z)$ is the comoving radial distance, $F(z)$ is the redshift evolution of clustering, N(z) is the survey selection function and

$$H_\gamma = \Gamma\left(\frac{1}{2}\right) \frac{\Gamma\left[(\gamma - 1)/2\right]}{\Gamma(\gamma/2)},$$

(4.4)

$$E(z) = \sqrt{\Omega_M (1 + z)^3 + \Omega_\Lambda},$$

(4.5)

where $\Gamma(x)$ is the gamma function $\gamma = \beta + 1$ (prescribed by Equation 4.2). Cosmological parameters are consistent with those assumed by previous KDF analyses: $(\Omega_M, \Omega_\Lambda, H_0) = (0.3, 0.7, 70\,\mathrm{km\,s^{-1}\,Mpc^{-1}})$.

The angular correlation function, A_ω, is measured directly from images with no assumptions about the volume from which the objects are projected and is thus independent of the presumed redshift distribution of the sample. Changes to the presumed model spectrum of the galaxy are reflected in N(z) which gives the distribution of galaxies observed in a survey per redshift interval. It is 0 outside the redshift range of the population and thus acts as a filter with a width corresponding to the redshift range permissible for member objects.

In their clustering analysis, Savoy et al. (2011) assumed that the KDF bBX galaxies (those in their bluest $z \sim 2.2$ $(G - \mathcal{R})$ colour bin) had Calzetti et al. (2000) dust with $E(B - V) = 0.15$, underwent constant star formation over their lives, were 10^8 years old and met the BX selection criteria (Equation 1.1) with no additional constraint on $G - \mathcal{R}$ colour (these ranges are given by the

union of the rBX and bBX regions and are shown as black bars in Figure 4.2). From the redshifted population synthesis models whose data are plotted in Figures 4.1 and 4.2, this gives a redshift range of $1.84 < z < 2.54$. The following calculations assume that this range gives the redshift integration limits used by Savoy et al. (2011) (i.e. N(z) is a tophat function with range $1.84 < z < 2.54$).

To determine the correction factor that applies to the correlation length calculated by Savoy et al. (2011) for each of the models included in the SEDfit grid, we relate the value of r_0 corresponding to their model with each new model by equating the Limber inversion calculations for both (thus exploiting the 2-dimensionality of A_ω). With the assumption that the redshift evolution of clustering is negligible over the ranges considered, we obtain the ratio of the BX and bBX spatial clustering results:

$$\frac{r_{0,\text{New Model}}}{r_{0,\text{Savoy}}} = \left(\left[\frac{\int_0^\infty r_c^{1-\gamma}(z)E(z)N_{\text{Savoy}}^2(z)dz}{\left[\int_0^\infty N_{\text{Savoy}}(z)dz\right]^2} \right] \left[\frac{\int_0^\infty r_c^{1-\gamma}(z)E(z)N_{\text{New Model}}^2(z)dz}{\left[\int_0^\infty N_{\text{New Model}}(z)dz\right]^2} \right]^{-1} \right)^{\frac{1}{\gamma}}.$$
(4.6)

This ratio was computed with $\gamma = 1.6$ and ΛCDM cosmology (as did Savoy et al. (2011)) and defining $N_{\text{New Model}}(z)$ as a tophat function $= 1$ in the redshift range where each model satisfies the bBX criteria and $= 0$ for other z. $N_{\text{Savoy}}(z)$ was similarly defined for the redshift range corresponding to BX selection (with no additional $(G - \mathcal{R})$ colour constraints) for the model they assumed. The results are summarized in Table 4.3 for all of the models and give the factor by which the Savoy et al. (2011) spatial correlation length must be multiplied to correct for the assumption of a new model so that values > 1 correspond to even stronger clustering and values < 1 correspond to a decreased clustering signal.

The correction factors found for the best fit model in each combination of SFH and dust law found in Section 2.4 are printed in bold in Tables 4.1,4.2, and 4.3. Because of time constraints and the computational cost of determining redshift ranges for the BX-selection of each model, the clustering correction factor was only calculated for half of the star formation histories considered

in Chapter 3. In Section 2.4, four models were found with only-slightly-higher χ^2 values than the global minimum χ^2 value and with marked consistency amongst their other parameters. Of these cases, the ratio was computed for the constant star formation ($r_{bBX}/r_{BX} = 0.39$) and exponentially decreasing star formation with $\tau = 1$ ($r_{bBX}/r_{BX} = 0.51$). Figure 4.3 shows the colour-dependence of the spatial clustering length found by Savoy et al. (2011). The ratio calculated here is the factor by which points corresponding to bBX objects should be reduced in Figure 4.3, however, the colour range over which this correction is applicable is unclear. The individual KDF bBX objects in the sample spanned a range of colours from $-0.09 \leq G - \mathcal{R} \leq 0.04$ which disagrees with the photometry of the average stacked object gives $G - \mathcal{R} = -0.21 \pm 0.03$ (if only background fluctuations are considered). The colours can also be considered from the redshift evolution of the best fit models to the stack photometry. As they progress through the bBX selection window shown in Figure 4.1, these models vary from $-0.20 \leq G - \mathcal{R} \leq -0.05$ ($\tau = 1$, MW dust, $E(B - V) = 0.15$, age $10^{8.5}$ yrs) and $-0.19 \leq E(B - V) \leq -0.10$. As the colour selection criterion becomes more extreme, it includes fewer objects of the objects in a given sample.

Since a minimum population size is necessary to measure clustering, Savoy et al. (2011) were only able to make direct clustering measurements for subsamples with $G - \mathcal{R} \geq 0$. The revised clustering result only applies directly to colours bluer than those shown in Figure 4.3. However, for all of the star formation histories included in the SEDfit model grid, the presence of a 2175Å absorption feature of any strength decreases the clustering strength measured for the bBX population. Observations of dust attenuation at high redshift suggest that there is no sharp divide between BX objects with the feature and those without (Noll & Pierini 2005). There is likely a smooth decrease in the prominence of the 2175Å feature relative to continuum absorption as the observed $(G - \mathcal{R})$ colour of galaxies becomes redder. If the ~ 0.45 value found for the correction factor to the spatial correlation length is valid for the bBXs around the threshold of $G - \mathcal{R} \sim 0.1$, the extreme rise in clustering strength with decreasing $(G - \mathcal{R})$ colour found for bBX objects by Savoy et al. (2011) may be reduced. With this correction factor applied, the relationship may be consistent with the dependence observed in the populations at $z \sim 3$ and $z \sim 4$.

SFH	Dust	Age	$E(B-V)$										
			0.00	0.05	0.10	0.15	0.20	0.25	0.30	0.35	0.40	0.45	0.50
Single Burst	Calzetti	6.0	-	1	1	0.99	0.82	0.11	0.11	-	-	-	-
		7.0	1	0.97	0.15	-	-	-	-	-	-	-	-
		7.5	1	0.11	-	-	-	-	-	-	-	-	-
		8.0	-	-	-	-	-	-	-	-	-	-	-
		8.5	-	-	-	-	-	-	-	-	-	-	-
	LMC	6.0	-	-	-	-	0.21	0.4	0.47	0.35	0.18	0.61	0.61
		7.0	1	1.06	0.98	0.8	0.46	0.12	-	-	-	-	-
		7.5	1	1	0.7	0.24	-	-	-	-	-	-	-
		8.0	-	-	-	-	-	-	-	-	-	-	-
		8.5	-	-	-	-	-	-	-	-	-	-	-
	MW	6.0	-	-	-	-	-	0.33	0.11	0.18	0.23	0.24	0.24
		7.0	1	1.07	0.27	0.5	0.47	0.47	0.39	0.36	0.31	-	-
		7.5	1	1.01	0.94	0.72	0.55	0.44	0.31	0.21	-	-	-
		8.0	-	-	-	-	-	-	-	-	-	-	-
		8.5	-	-	-	-	-	-	-	-	-	-	-

Table 4.1: Fractional change in physical correlation length from redshift ranges of bBX-selection for various models with a single burst star formation history. For each combination of dust, age, $E(B-V)$, the redshift range over which a galaxy with the same SFH, and age but Calzetti dust meets the BX selection criteria is compared to the redshift range over which a galaxy with the listed dust law meets the bBX selection criteria. Dashes indicate models which do not meet the bBX and/or the BX selection criteria at any redshift considered.

This analysis has not considered whether a more appropriate parametrization of dust attenuation exists for redder BX galaxies or for galaxies at lower redshift. Finding better models for these objects could also change their inferred spatial clustering. As it stands, the reversal of the relationship between clustering strength and rest-frame UV colour is still possible, but may occur at lower redshift than previously believed. Better knowledge of the time evolution of this relationship will point us to the population we must observe in order to understand the peak in star formation observed at $z \sim 2.2$. This understanding will only be acquired if models with more flexible dust attenuation parametrizations, such as that of Buat et al. (2011), are applied to populations at all redshifts.

SFH	Dust	Age	$E(B-V)$										
			0.00	**0.05**	**0.10**	**0.15**	**0.20**	**0.25**	**0.30**	**0.35**	**0.40**	**0.45**	**0.50**
		6.0	-	1	1	0.99	0.84	0.11	0.11	-	-	-	-
		7.0	1	1	0.96	0.34	-	-	-	-	-	-	-
	Calzetti	**7.5**	1	1	0.88	-	-	-	-	-	-	-	-
		8.0	1	0.97	0.22	-	-	-	-	-	-	-	-
		8.5	1	0.83	**-**	-	-	-	-	-	-	-	-
		6.0	-	-	-	-	0.21	0.4	0.47	0.35	0.18	0.61	0.61
		7.0	1	0.3	0.16	0.51	0.73	0.53	0.28	0.12	-	-	-
Constant SF	LMC	**7.5**	1	0.77	0.99	0.85	0.65	0.41	0.19	-	-	-	-
		8.0	1	1.02	0.95	**0.79**	0.5	0.24	0.06	-	-	-	-
		8.5	1	1	0.9	0.63	0.31	-	-	-	-	-	-
		6.0	-	-	-	-	-	0.33	0.11	0.18	0.23	0.24	0.24
		7.0	1	0.15	-	-	0.18	0.24	0.29	0.34	0.29	0.3	1.41
	MW	**7.5**	1	0.25	0.15	0.19	0.29	0.34	0.39	0.35	0.36	0.47	-
		8.0	1	0.48	0.16	**0.39**	0.41	0.41	0.38	0.34	0.3	-	-
		8.5	1	1.01	0.43	0.51	0.49	0.4	0.38	0.33	0.29	-	-

Table 4.2: Fractional change in physical correlation length from redshift ranges of bBX-selection for various models with constant star formation. For each combination of dust, age, $E(B-V)$, the redshift range over which a galaxy with the same SFH, and age but Calzetti dust meets the BX selection criteria is compared to the redshift range over which a galaxy with the listed dust law meets the bBX selection criteria. Dashes indicate models which do not meet the bBX and/or the BX selection criteria at any redshift considered.

SFH	Dust	Age	$E(B-V)$										
			0.00	**0.05**	**0.10**	**0.15**	**0.20**	**0.25**	**0.30**	**0.35**	**0.40**	**0.45**	**0.50**
Constant SF	Calzetti	**6.0**	-	1	1	0.99	0.84	0.11	0.11	0.12	-	-	-
		7.0	1	1	0.96	0.41	-	-	-	-	-	-	-
		7.5	1	1	0.9	-	-	-	-	-	-	-	-
		8.0	1	0.98	0.31	-	-	-	-	-	-	-	-
		8.5	1	**0.85**	**-**	-	-	-	-	-	-	-	-
	LMC	**6.0**	-	-	-	-	0.21	0.4	0.47	0.35	0.18	0.61	0.61
		7.0	1	0.31	0.16	0.51	0.68	0.56	0.33	0.12	-	-	-
		7.5	1	0.68	0.99	0.85	0.68	0.41	0.19	-	-	-	-
		8.0	1	1.04	0.97	**0.83**	0.53	0.29	-	-	-	-	-
		8.5	1	1	0.9	0.63	0.31	-	-	-	-	-	-
	MW	**6.0**	-	-	-	-	-	0.29	0.11	0.18	0.23	0.24	0.24
		7.0	-	-	-	0.13	0.18	0.24	0.29	0.34	0.29	0.25	1.1
		7.5	-	-	-	0.19	0.29	0.34	0.39	0.35	0.36	0.43	2.73
		8.0	0.14	0.12	0.1	0.33	0.41	0.41	0.38	0.34	0.3	1.09	-
		8.5	-	-	0.37	**0.51**	0.49	0.4	0.38	0.34	0.29	2.13	-

Table 4.3: Fractional change in physical correlation length from redshift ranges of bBX-selection for various models with exponentially declining star formation with $\tau = 1$. For each combination of dust, age, $E(B - V)$, the redshift range over which a galaxy with the same SFH, and age but Calzetti dust meets the BX selection criteria is compared to the redshift range over which a galaxy with the listed dust law meets the bBX selection criteria. Dashes indicate models which do not meet the bBX and/or the BX selection criteria at any redshift considered.
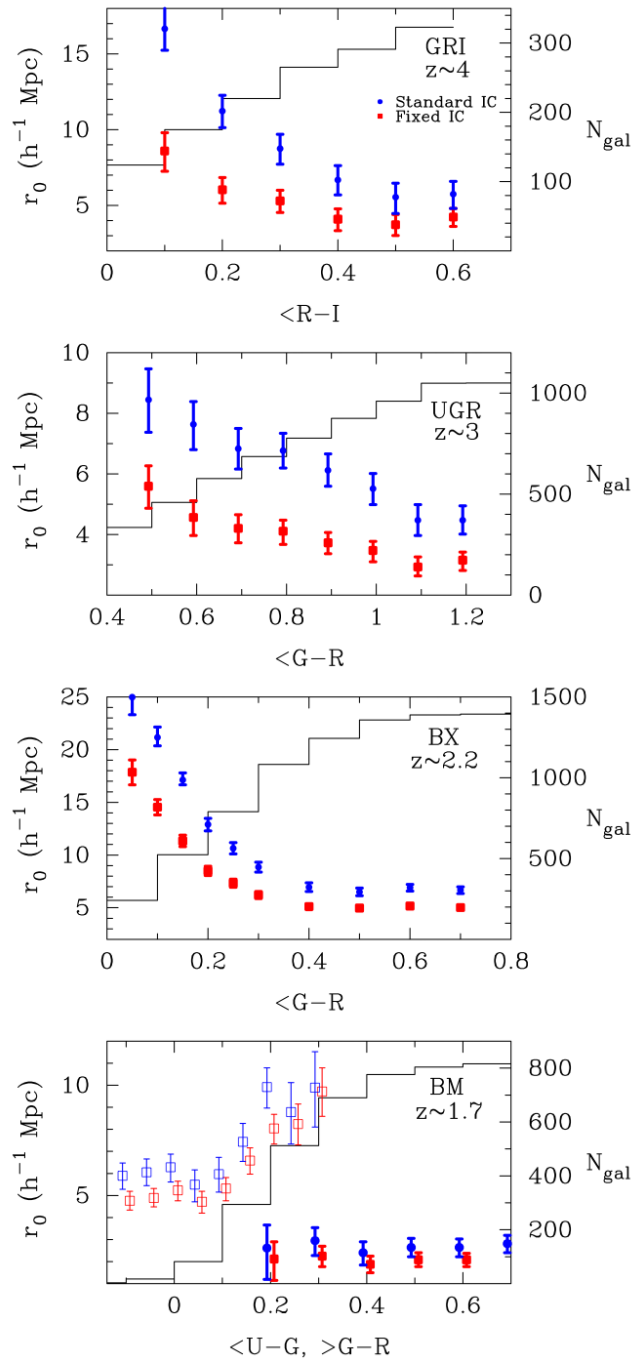
Figure 4.3: Spatial correlation length as a function of rest frame UV colour for the 4 redshift selection ranges used in the KDF analysis as presented by Savoy et al. (2011). In each panel red and blue data sets correspond to extreme values of the integral constraint which corrects for the limited size of the field over which the statistic is computed. In the fourth panel, squares represent the total number of objects with colours redder the corresponding value.

4.2 The 2175Å Feature as a Redshift Indicator

The average of the best fit redshifts found from the SED fitting procedure described in Section 3.4 agrees with the expected redshifts of BX galaxies as a whole. The characteristic redshift was recovered by fitting only the *GRI* photometry of the bBX objects in the KDF sample. This is particularly impressive because neither of the spectral features typically relied upon to determine redshifts in this range (the Lyman and Balmer/4000Å breaks) were captured in these data.

If a single model SED at a precise redshift with one of the dust laws considered were a perfect representation of each and every one of the bBX galaxies, there would be a tight correlation between these two parameters. The $G - \mathcal{R}$ colour would change with the depth of the 2175Å feature which is determined by the amount of dust present. Figure 3.4 plots the best fit model $E(B - V)$ for each object against its observed $G - \mathcal{R}$ colour. Despite the striking success of the SEDfit best fit model redshifts in recovering the mean redshift of BX galaxies, no correlation is apparent. This lack of correlation reflects poor sampling resolution of the spectra of the objects in the region of the bump. If the *G*-band photometry sampled the continuum level of the spectra and the central wavelength of the $\mathcal{R}$ filter was located at the precise minimum of the 2175Å feature for every object, a strong dependence of best fit $E(B - V)$ on rest frame UV colour would be expected. Because of the intrinsic distribution of redshifts for bBX objects, the wavelength of maximum absorption in the bump is also a distribution.

For both the MW and LMC dust laws the width of the 2175Å feature is independent of $E(B - V)$. It should therefore be possible to determine the central wavelength of the bump and its depth relative to the continuum spectrum from observations at four wavelengths: two intended to measure the continuum at wavelengths longer and shorter than the 2175Å feature and two at wavelengths affected by the bump. The addition of a single additional observation to the *GRI* photometry of the KDF survey would likely permit much more precise redshift determination for galaxies with a 2175Å feature.

To investigate how successful this technique might be, SEDfit was used to fit simulated

photometry of model spectra at known redshifts with one new filter in addition to the *GRI* used in the

KDF survey. The additional filter, denoted R^+, has central wavelength of 7300Å. Its transmission

function is show in Figure 4.4 along with those of the *GRI* filters used in the KDF survey and the

spectrum of a model galaxy at z = 2.2 with physical properties consistent with those of the best fit

to the average stack bBX object.

A catalog of model galaxy spectra was created with the SEDfit program `make_bbsed` which

takes rest-frame population synthesis models and applies effects to simulate observations of the

galaxy at z > 0. The galaxies have constant star formation, MW dust with values of $E(B-V)$

ranging from 0.0 to 0.7 and masses comparable to the best fits to the stacked bBX data. The model

spectra were convolved with the 5 filter transmission curves plotted in Figure 4.4 at redshifts from

2.0 to 2.4 (although as in the analysis of Section 3.4, the U_n data were excluded from the fits). The

model magnitudes were then normalized to $\mathcal{R}_{AB}$=25.97, the value found for the average stacked

bBX object. Photometric uncertainties were then assigned to each simulated photometric data point

consistent with those of KDF bBX objects with similar magnitudes. SEDfit was run on each set of

photometry to see how accurately redshifts could be recovered.

SEDfit was run twice on the catalog of simulated galaxies, comparing the photometric data to

a grid of models for constant star formation with MW dust over the redshift range $1.6 <$ z < 3.0

with $0 < E(B-V) < 1.0$. In the first set of fits, only the *GRI* photometry was considered, as in

the analysis of KDF objects described in Chapter 3. The fits were then repeated with the $GRIR^+$

photometry. Figure 4.5 compares the redshifts of the simulated data to the corresponding best fit

model redshifts for each SEDfit run. With the data from the three filters used in the analysis of the

KDF bBX objects, there is a large scatter in the result but no bias toward over or under-predicting

redshifts. This is consistent with the result of Section 3.4 which found an average best fit redshift

of the KDF bBX sample in agreement with that expected for BX-selected objects in general. The

addition of the R^+ filter with central wavelength 7300Å dramatically increases the accuracy of best

fit model redshifts for individual objects. Figure 4.6 compares the ratio z_{fit}/z_{true} to $E(B-V)$.

There is no apparent correlation between the success of redshift recovery and the amount of dust in

Figure 4.4: Transmission functions of filters used to test the usefulness of the 2175Å dust feature as a redshift indicator independent of the Lyman and Balmer discontinuities and the spectrum of a $z \sim 2.1$ galaxy with MW dust. The $U_n G\mathcal{R}I$ curves correspond to the filters used for the KDF observations. The FTC labelled $\mathcal{R}^+$ is an additional filter used in simulated observations to test 2175Å feature's usefulness as a redshift indicator. Its transmission function is that of the G filter translated to a central wavelength of 7500Å.
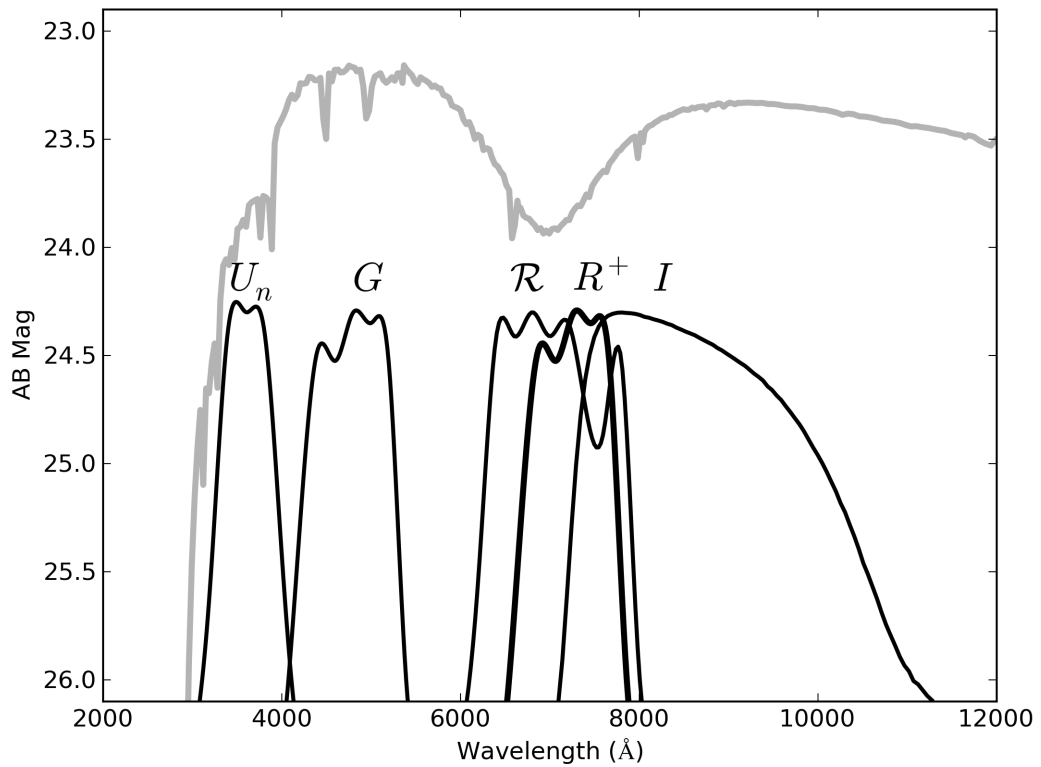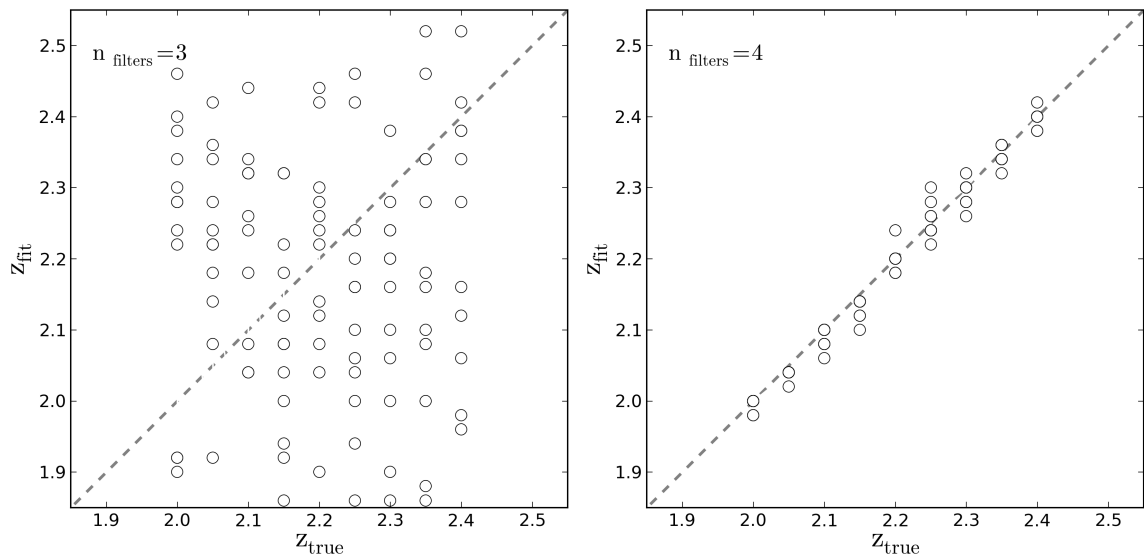
Figure 4.5: Comparison of simulated galaxy data to the best fit model redshift found by SEDfit using data from the 3 filters used in the analysis described in Section 3.4 (left) and using the addition $\mathcal{R}^+$ filter.

a galaxy, suggesting that the 2175Å feature could be used very effectively to measure photometric redshifts of individual bBX-selected objects over a wide range of dust content fractions with just one additional filter.

While it is clear that many of the bBX galaxies in the KDF sample are best modeled by a dust law that includes a 2175Å feature, the question of whether the LMC or MW dust (or something completely different) is most appropriate for modeling attenuation has not been resolved. Figures 4.5 and 4.6 demonstrate that the feature is useful in determining the redshift of a galaxy when both the data and model grid are drawn from spectra with precisely MW dust. To investigate whether or not the choice of 2175-indcluding dust law might affect the success of redshift recovery, the SED fitting procedure was repeated on the simulated data for galaxies with MW dust, but this time fit to a model grid which included only spectra with LMC dust. Figure 4.8 compares the true redshifts of simulated data to the best fit model redshifts, analogous to Figure 4.5. In this case, galaxies at $z \sim 2.2$ (generally cited as the mean redshift of BX objects) are reasonably fit by either dust law with the addition of the R^+ filter. At lower redshift, z_{fit} is systematically overestimated and at
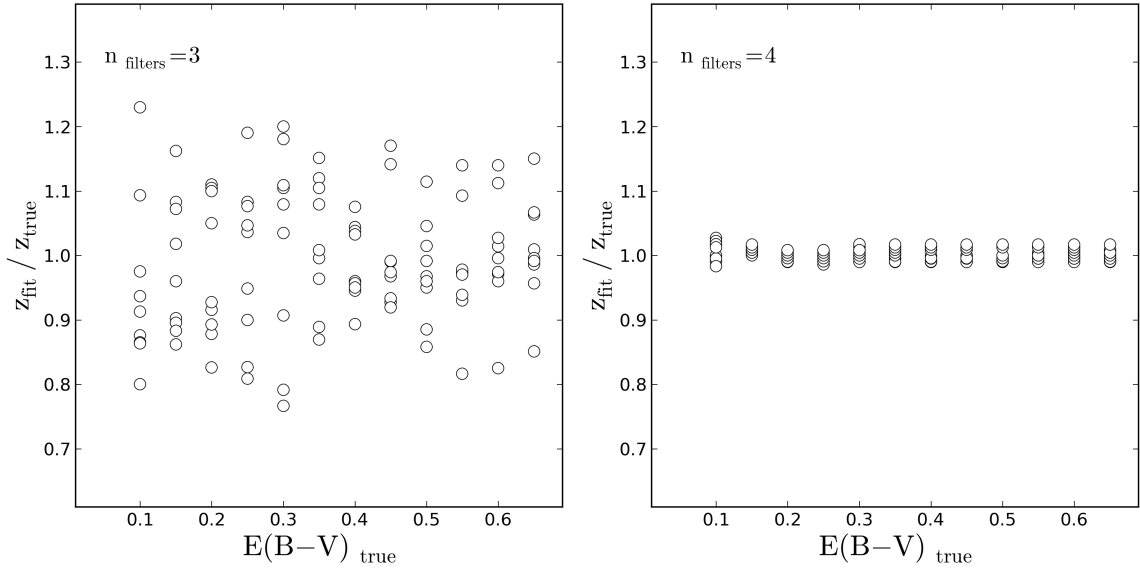
Figure 4.6: Comparison of the ration $\frac{z_{fit}}{z_{true}}$ to the 'true' value of $E(B-V)$ found by SED fitting to a model grid only containing MW dust models using data from the 3 filters used in the analysis described in Section 3.4 (left) and using the additional $\mathcal{R}^+$ filter (right).

higher redshift z_{fit} is underestimated. This can be explained by the difference in amplitude of the 2175Å bump in the two dust laws relative to their respective continuum extinction levels, as seen in the first panel of Figure 4.7. The shallower relationship than the expected 1:1 correlations in both the 3 and 4 filter cases in Figure 4.9 means that regardless of a galaxy's true redshift, SEDfit places it at the same redshift. When significant MW dust is included in a model, the $G - \mathcal{R}$ colour produced by its attenuation will be bluer than exists for any two points in the spectrum of a galaxy with LMC dust separated by the same distance as the G and $\mathcal{R}$ filters in wavelength space. The best fitting model will simply be one at the redshift that maximizes the $G - \mathcal{R}$ colour, around $z \sim 2.2$. This degeneracy suggests that parametrizations of dust attenuation that allow the 2175 feature and continuum absorption to differ independently, such as those employed by Buat et al. (2011), may be much more successful for inferring physical parameters of high redshift galaxies for which 1-parameter dust laws cannot be determined.

The scatter in the ratio z_{fit}/z_{true} appears to increase symmetrically at redshifts above and below $z \sim 2.2$. Figure 4.9 compares the ratio to the dust content fraction of the model galaxies, analogous
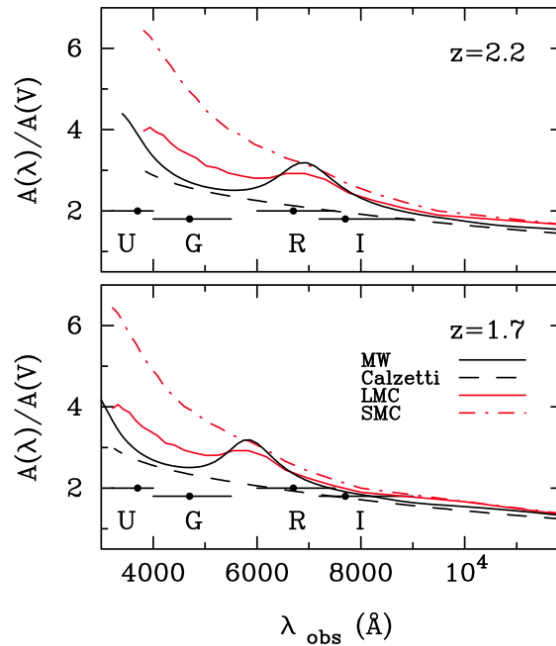
Figure 4.7: Calzetti, LMC, and MW dust laws relative to $UG\mathcal{R}I$ filter central wavelengths at $z \sim 2.2$ and $z \sim 1.7$, as presented by Savoy et al. (2011) (used with permission)

to Figure 4.6. At low values of $E(B-V)$, z_{fit}/z_{true} approaches a 1:1 relationship. This can be attributed to the amplitude of the dust feature becoming comparable to the photometric uncertainty ($\sigma_{AB} \sim 0.1$). i.e. when $E(B-V) = 0$, no dust is present and the result is the same independent of the dust law included in the model.

The 2175Å feature can have a prominent effect on the spectra of galaxies when it is present. The exercise described above shows that it could be very useful in constraining the redshifts of objects where it is known to be present. A possible difficulty in efficiently exploiting the bump is that its existence must be known a priori if it is to be used alone for redshift determination (as was the case in the idealized redshift recovery scenario described here). Within the BX population, the rest-frame UV colour of objects might be a useful indicator in predicting the type of dust law appropriate for a galaxy. However, more work must be done to properly characterize the dust in these objects to determine the potential usefulness of the 2175Å feature.
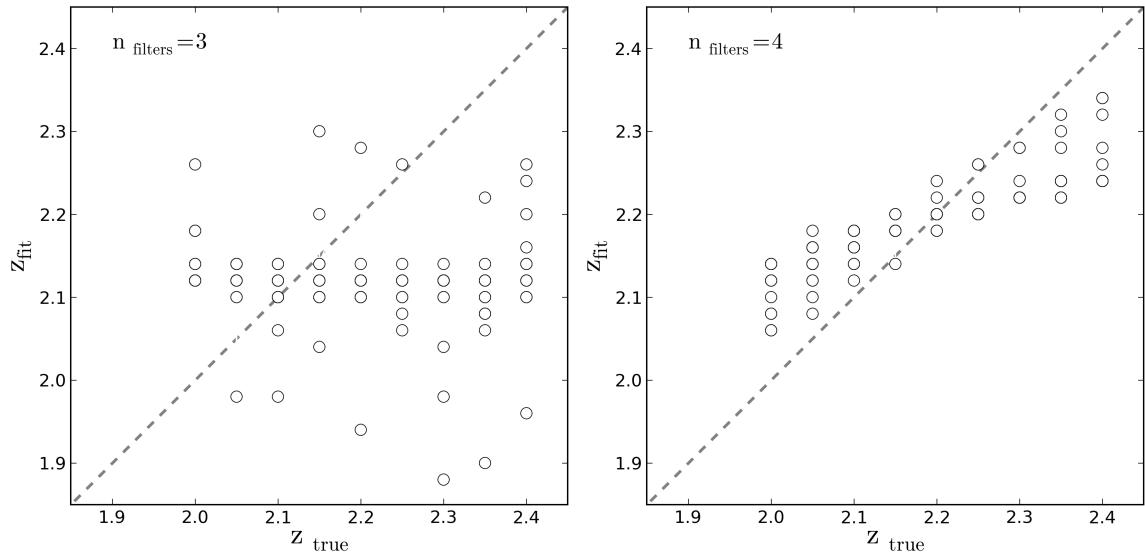
Figure 4.8: Comparison of the 'true' redshifts of simulated galaxies with MW dust to the best model redshift found by SED fitting to a model grid only containing LMC dust models using data from the 3 filters used in the analysis described in Section 3.4 (left) and using the addition $\mathcal{R}^+$ filter (right).
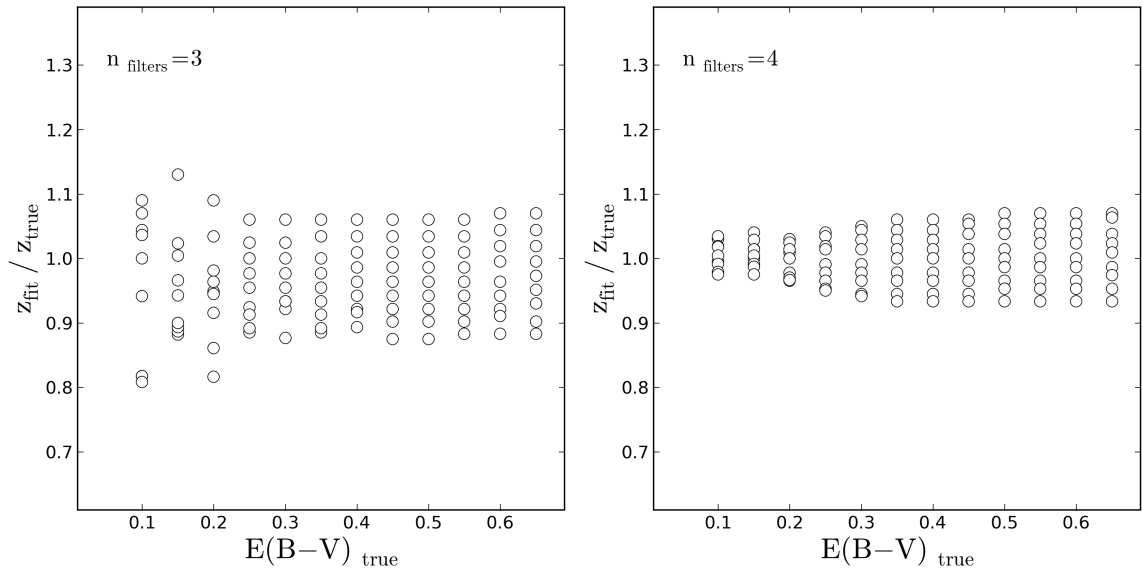

Figure 4.9: Comparison of the ration $\frac{z_{fit}}{z_{true}}$ to the 'true' value of $E(B-V)$ found by SED fitting to a model grid only containing LMC dust models using data from the 3 filters used in the analysis described in Section 3.4 (left) and using the addition $\mathcal{R}^+$ filter (right).

Chapter 5

Discussion and Conclusions

5.1 Physical Properties of bBX Galaxies

Savoy et al. (2011) suggested that the most massive, most strongly clustered galaxies at $z \sim$ 2.2 are those with the oldest stellar populations and prominent 2175Å dust features (giving rise to their blue colours). The initial objective of the analysis described in this thesis was to test their hypothesis by comparing the masses and ages of the bBX objects to BX objects in general. The very deep observations of the KDF observations provide data from a sample of BX objects that includes galaxies much fainter than any other survey. This allowed a more accurate determination of the high redshift luminosity function and measures of star formation (Sawicki & Thompson 2006a) than had previously been possible. The existing rest-frame UV observations of the KDF were insufficient to precisely infer masses and ages of member BX objects so IR observations were performed in order to measure the magnitude of the Balmer break in this sample. For reasons unknown (despite exhaustive efforts to find an error in the data reduction and photometry procedures) these data were not sufficiently deep to detect the majority of BX-selected objects. Without these IR detections it is impossible to determine the masses or ages of these objects with the precision necessary to differentiate between the rBX and bBX populations if, indeed, the difference proposed by Savoy et al. (2011) exists.

An alternative method of testing the hypothesis of Savoy et al. (2011) was pursued by SED fitting to the $G\mathcal{R}I$ photometry for individual KDF bBX objects. More dust laws were included in the SED fitting model grid than had been employed in prior analyses of these data. The results showed that, indeed, many of the bBX objects are better represented by models with a dust attenuation law that includes the 2175Å feature than by those using the conventionally assumed Calzetti et al. (2000). The most flexible parametrization of dust attenuation at high redshift is a general dust law in which the continuum slope and 2175Å feature strength vary independently. For concreteness in this work, two familiar dust laws from the local universe in which the feature is pronounced were used. Buat et al. (2012a) and Noll et al. (2007a) employ multicomponent models and find them to be successful in describing the observed properties of high redshift galaxies. Their results suggest that the the shape of the 2175Å bump at $z \sim 2$ lies somewhere between the pronounced feature of the MW model and its smoother LMC counterpart.

5.2 Clustering of bBX Objects

The curiously strong clustering strength of the bluest BX galaxies observed by Savoy et al. (2011) served as the impetus for the hypothesis that they were older and more massive than their contemporaries and display a 2175Å dust feature. Their clustering analysis assumed that the objects were constantly star forming, 10^8 years old and contained Calzetti et al. (2000) dust with $E(B - V) = 0.15$. This model choice gave the volume used in the deprojection of the angular clustering measured from the KDF images (i.e. the width of the tophat function, N(z), in Equation 4.3).

Section 4.1 examined the extent to which the redshift range over which a galaxy meets the BX selection criteria is affected by varying its presumed rest-frame model. This effect has not previously been examined but the results of the analysis described in this thesis show that it may have a large impact on clustering results. Using the parameters of the best fit models found for the average stacked bBX object (all of which include non-Calzetti dust) revised redshift ranges for the bBX populations were determined by redshifting each model spectrum and checking it against the bBX

criteria at intervals $\Delta z = 0.01$. For each redshift range, Equation 4.1 was used to estimate the factor by which the spatial correlation length found in the original KDF clustering analysis would change with the assumption of the new model.

The results suggest that the correlation lengths of bBX populations found by Savoy et al. (2011) might overestimate the r_0 by more than a factor of 2. Taking this into consideration, the observed correlation between UV colour and clustering strength may be reduced to a level consistent with no evolution between $z \sim 3$ and $z \sim 2.2$, as show in Figure 4.3. If this is the case, then the bBX objects are not likely to provide direct evidence of the shutdown of star formation at $z \sim 2$.

However, the results found here should be taken with a grain of salt. The best fit models to the photometry of the average stacked bBX object contain MW dust. These models have colours of $G - \mathcal{R} \sim -0.2$: well beyond the bluest subsample analyzed by Savoy et al. (2011). This is the colour at which the factor of two correction found here is applicable. To determine the true impact of revising dust laws and redshift ranges, the entire clustering analysis would need to be redone, an endeavour well beyond the scope of this project. The possibility that drastically different results may be obtained extends to all high redshift clustering studies which assume Calzetti et al. (2000) dust.

5.3 Future Work

The SED fitting analysis described in Chapter 3 supports the presence of the 2175Å feature in bBX galaxies. As such, the intriguing possibility that these objects are more massive than others at the same redshift remains open despite the doubt cast on their strong clustering in Section 4.1. Obtaining deeper IR observations of the fields and performing this analysis again could yield important results. The inference of physical parameters for a specific object is heavily dependent on the accuracy with which its redshift can be determined. To perform this analysis more robustly, spectroscopic redshifts, such as those available for the objects studied by Erb et al. (2006) could be obtained.

Additional photometry in a fourth filter in the region of the bump, as considered in Section 4.2, may provide a less observationally expensive alternative to spectroscopy. In Section 4.2, four photometric data points were found to dramatically improve the rate of redshift recovery for simulated observations. However, this technique was less successful when the precise parametrization of the dust law was not known a priori. The four-filter photometry route to increasing redshift precision seems promising for high redshift galaxies whose spectra show a 2175Å feature, but more work must be done to determine the functional form of dust attenuation in bBX galaxies before its full potential is realized. Observations with even more filters could certainly improve results even more, but the trade off between efficiency in obtaining data and the precision of results must be considered.

The question of whether or not the strong colour dependence of clustering strength at $z \sim 2$ is real presents another interesting puzzle to investigate. Figure 4.2 shows that the redshift ranges of rBX and bBX galaxies can be very different. To gain insight into the colour-dependence of clustering at $z \sim 2$, it will be necessary to calculate the appropriate redshift range for each colour bin in the sample individually after determining the best model for member objects. Measuring the clustering of the the bluest groups of galaxies in the BX sample is complicated by the increasing paucity of member objects as more and more stringent criteria of blueness are required. It was for this reason that the bluest $z \sim 2$ subsample included by Savoy et al. (2011) has $G - \mathcal{R} \sim 0.05$. Deeper rest-frame UV observations of a much wider field than the KDF will be required to directly measure the correlation of UV colour and clustering strength in the objects to $G - \mathcal{R} \sim -0.2$.

5.4   Final Remarks

As do most scientific inquiries, this investigation into the anomalous clustering observed for bBX galaxies has opened many new questions and definitively answered none. While the Gemini observations intended to constrain the masses and ages of the bBX galaxies were of lower quality than required to meet their science goals, reanalyzing the *UGRI* data in the KDF catalog led to

unanticipated insights. The results of SED fitting to these data (both for the individual objects and the single object created by stacking their images) permitting more dust laws than were previously considered suggest that the standard issue Calzetti et al. (2000) dust attenuation model is inappropriate for use in modeling many bBX galaxies. Dust laws including a 2175Å feature were also found to improve the quality of fits for a significant number of bBX galaxies with $H\alpha$ redshifts studied by Erb et al. (2006).

Finding that many of the bBX galaxies are better represented by models with MW or LMC dust motivated a reexamination of the clustering analysis of Savoy et al. (2011). The redshift ranges over which the best fitting models would meet the bBX selection criteria can be very different from those assumed in the original analysis. For the bluest colour bins considered by Savoy et al. (2011), this may cause spatial correlation lengths to be overestimated by more than a factor of two.

Recent studies of dust in high redshift galaxies find the 2175Å feature to be common in these populations and suggest that it is necessary to consider this feature separately from continuum dust attenuation when modeling high redshift objects (Buat et al. 2012b). The colour cut of G-$\mathcal{R} < 0.1$ defining bBX objects in this analysis is arbitrary so it is likely that the clustering of objects with redder rest-frame UV colours will be altered to some degree as well. A factor of two decrease in the clustering strength of the bluest colour bins in of the sample considered by Savoy et al. (2011) could eliminate the observed evolution of the relationship between rest-frame UV colour and spatial correlation length between $z \sim 3$ and $z \sim 2.2$, casting doubt on this result and the many other analyses that blindly assume Calzetti et al. (2000) dust attenuation. The deleterious effect of incorrect model assumption is not limited to clustering measurements, but may affect any physical quantity inferred from photometric data including star formation rates, chemical compositions, ages, masses and temperatures of individual objects and on larger scales, mass and luminosity functions and luminosity, star formation and mass densities. It is crucial to carefully consider the dust attenuation properties of an object and the way their variation might impact the final result of any high redshift analysis. It should be possible to use currently available data sets to perform analyses similar to that carried out here to develop a better understanding of dust properties at high redshift.

Bibliography

Adelberger, K. L., Steidel, C. C., Shapley, A. E., et al. 2004, The Astrophysical Journal, 607, 226

Bertin, E. & Arnouts, S. 1996, Astronomy and Astrophysics Supplement Series, 117, 393

Bourne, N., Maddox, S. J., Dunne, L., et al. 2012, Monthly Notices of the Royal Astronomical Society, 421, 3027

Bruzual, G. & Charlot, S. 2003, Monthly Notices of the Royal Astronomical Society, 344, 1000

Buat, V., Giovannoli, E., Heinis, S., et al. 2011, Astronomy & Astrophysics, 533, A93

Buat, V., Noll, S., Burgarella, D., et al. 2012a, Astronomy & Astrophysics, 545, A141

Buat, V., Noll, S., Burgarella, D., et al. 2012b, Astronomy & Astrophysics, 545, A141

Calzetti, D., Armus, L., Bohlin, R. C., et al. 2000, The Astrophysical Journal, 533, 682

Daddi, E., Dickinson, M., Morrison, G., et al. 2007, The Astrophysical Journal, 670, 156

Erb, D. K., Steidel, C. C., Shapley, A. E., et al. 2006, The Astrophysical Journal, 646, 107

Finlator, K., Oppenheimer, B. D., & Davé, R. 2010, Monthly Notices of the Royal Astronomical Society, 410, 1703

Fitzpatrick, E. 1999, Publications of the Astronomical Society of the Pacific, 111, 63

Fitzpatrick, E. L. 1986, The Astronomical Journal, 92, 1068

Guaita, L., Acquaviva, V., Padilla, N., et al. 2011, The Astrophysical Journal, 733, 114

Guhathakurta, P., Tyson, J. A., & Majewski, S. R. 1990, The Astrophysical Journal, 357, L9

Hodapp, K. W., Jensen, J. B., Irwin, E. M., et al. 2003, Publications of the Astronomical Society of the Pacific, 115, 1388

Hopkins, A. M. & Beacom, J. F. 2006, The Astrophysical Journal, 651, 142

Ilbert, O., Capak, P., Salvato, M., et al. 2009, The Astrophysical Journal, 690, 1236

Iwata, I., Ohta, K., Tamura, N., et al. 2007, Monthly Notices of the Royal Astronomical Society, 376, 1557

Jaacks, J., Nagamine, K., & Choi, J.-H. 2012, Monthly Notices of the Royal Astronomical Society, 427, 403

Kriek, M., van Dokkum, P. G., Whitaker, K. E., et al. 2011, The Astrophysical Journal, 743, 168

Landy, S. D. & Szalay, A. S. 1993, The Astrophysical Journal, 412, 64

Lee, K.-s., Giavalisco, M., Gnedin, O. Y., et al. 2006, The Astrophysical Journal, 642, 63

Leggett, S. K., Currie, M. J., Varricatt, W. P., et al. 2006, 792, 781

Madau, P. 1995, The Astrophysical Journal, 441, 18

Madau, P. & Pozzetti, L. 1998, 1, 106

Magnelli, B., Elbaz, D., Chary, R. R., et al. 2009, Astronomy and Astrophysics, 496, 57

Massa, D., Fitzpatrick, E. L., & Savage, B. D. 1982, NASA. GSFC Advances in Ultraviolet Astronomy, 409

Michalowski, M. J., Dunlop, J. S., Ivison, R. J., et al. 2012, Monthly Notices of the Royal Astronomical Society, 426, 1845

Mo, H., Jing, Y., & White, S. 1996, Monthly Notices of the Royal Astronomical Society, 282, 1096

Noll, S. & Pierini, D. 2005, Astronomy and Astrophysics, 155, 137

Noll, S., Pierini, D., Pannella, M., & Savaglio, S. 2007a, Astronomy and Astrophysics, 472, 455

Noll, S., Pierini, D., Pannella, M., & Savaglio, S. 2007b, Astronomical Society of the Pacific Conference Series, 380, 461

Ouchi, M., Shimasaku, K., Okamura, S., et al. 2004, The Astrophysical Journal, 611, 660

Reddy, N. A., Erb, D. K., Steidel, C. C., et al. 2005, The Astrophysical Journal, 633, 748

Salim, S., Dickinson, M., Michael Rich, R., et al. 2009, The Astrophysical Journal, 700, 161

Salpeter, E. E. 1955, The Astrophysical Journal, 121, 161

Savage, B. D. 1975, The Astrophysical Journal, 199, 92

Savoy, J., Sawicki, M., Thompson, D., & Sato, T. 2011, The Astrophysical Journal, 737, 92

Sawicki, M. 2012, Publications of the Astronomical Society of the Pacific, 124, 1208

Sawicki, M. & Thompson, D. 2005, The Astrophysical Journal, 635, 100

Sawicki, M. & Thompson, D. 2006a, The Astrophysical Journal, 642, 653

Sawicki, M. & Thompson, D. 2006b, The Astrophysical Journal, 648, 299

Shapley, A. E., Steidel, C. C., Erb, D. K., et al. 2005, The Astrophysical Journal, 626, 698

Stecher, T. P. 1969, The Astrophysical Journal, 157, L125

Steidel, C. C., Giavalisco, M., Dickinson, M., & Adelberger, K. L. 1996, The Astronomical Journal, 112, 352

Steidel, C. C., Pettini, M., & Hamilton, D. 1995, The Astronomical Journal, 110, 2519

Steidel, C. C., Shapley, A. E., Pettini, M., et al. 2004, The Astrophysical Journal, 604, 534

Tielens, A. 2008, Annual Review of Astronomy and Astrophysics, 46, 289

Tokunaga, A. T. & Vacca, W. D. 2005, Publications of the Astronomical Society of the Pacific, 117, 421

Totsuji, H. & Kihara, T. 1969, Publications of the Astronomical Society of Japan, 21, 221

Wake, D. A., Whitaker, K. E., Labbé, I., et al. 2011, The Astrophysical Journal, 728, 46

Walcher, C. J., Boker, T., Charlot, S., et al. 2006, The Astrophysical Journal, 649, 692

Zhao, Y., Gu, Q., & Gao, Y. 2011, The Astronomical Journal, 141, 68